

Unsupervised machine learning shock capturing for High-Order CFD solvers

Andrés Mateo-Gabín,^{1, a)} Kenza Tlaes,¹ Eusebio Valero,^{1,2} Esteban Ferrer,^{1,2} and Gonzalo Rubio^{1,2}

¹⁾*ETSIAE-UPM-School of Aeronautics, Universidad Politécnica de Madrid, Madrid-Spain*

²⁾*Center for Computational Simulation, Universidad Politécnica de Madrid, Madrid-Spain*

(Dated: 2 August 2023)

We present a novel unsupervised machine learning shock capturing algorithm based on Gaussian Mixture Models (GMMs). The proposed GMM sensor demonstrates remarkable accuracy in detecting shocks and is robust across diverse test cases without the need for parameter tuning. We compare the GMM-based sensor with state-of-the-art alternatives. All methods are integrated into a high-order compressible discontinuous Galerkin solver where artificial viscosity can be modulated to capture shocks. Supersonic test cases, including high Reynolds numbers, showcase the sensor's performance, demonstrating the same effectiveness as fine-tuned state-of-the-art sensors. The adaptive nature and ability to function without extensive training datasets make this GMM-based sensor suitable for complex geometries and varied flow configurations. Our study reveals the potential of unsupervised machine learning methods, exemplified by the GMM sensor, to improve the robustness and efficiency of advanced CFD codes.

^{a)}Electronic mail: andres.mgabin@upm.es.

I. INTRODUCTION

Shock waves are complex and significant fluid phenomena in engineering, observed, for example, in high-speed transport or in combustion and detonation processes¹. High-speed flows exhibit a combination of smooth regions and thin regions with abrupt changes in flow properties.

To effectively handle the various scales present in these flows, it is necessary to employ robust and computationally efficient numerical schemes that maintain a high level of precision². Standard discretizations for smooth flows may exhibit oscillations when shocks are present, and require special techniques for shock regularization within designated regions². The shock-fitting approach, which explicitly tracks and fits shock waves, is one method used to handle shocks³⁻⁵. However, the utilization of shock fitting is limited, primarily due to the difficulties it presents when applied to unstructured grids. An alternative and more commonly employed approach is the use of shock-capturing methods. The choice of the baseline discretization scheme determines the availability of various shock-capturing approaches. For finite volume discretizations⁶, typical options include TVD limiting strategies⁷ or essentially non-oscillatory (W)ENO reconstructions⁸⁻¹⁵. In the case of flux reconstruction (FR)^{16,17} and discontinuous Galerkin (DG)¹⁸ schemes, the methods generally fall into two categories. The first category involves the local switching of the discretization operator to a more robust one, achieved through h-refinement and/or p-coarsening. By employing appropriate limiting techniques, this operator ensures both accuracy and solution boundedness. Noteworthy references related to this category include 19–29. A similar approach involves performing a hybrid blending with a low-order subcell variant of the scheme³⁰⁻³³. In the second category, known as the artificial viscosity shock-capturing method, a local diffusion operator with a predetermined strength is introduced to regularize the solution once a shock is detected. Prominent examples of this approach can be found in the references 34–45.

Regardless of the specific method used, accurately determining the precise location of shock waves is of paramount importance. This becomes particularly critical since shock regularization methods tend to introduce excessive dissipation in smooth regions, potentially leading to loss of accuracy. This task itself is generally accomplished using parameter-dependent indicator functions derived from physical considerations⁴⁶, modal smoothness estimates^{38,47,48}, or image detection concepts⁴⁹⁻⁵³. An inherent limitation of all sensors is

the requirement for manual adjustment of numerical parameters. An improper configuration of these parameters can potentially lead to simulation failures or crashes. In recent years, machine learning (ML) techniques have become increasingly integrated into natural sciences and engineering, as evident in references 54–56. This trend has also extended to the field of computational fluid dynamics (CFD), where numerous successful applications of ML have emerged. The current state and future prospects of ML in fluid mechanics have been extensively discussed in references 56–60. Shock capturing is no exception, and one popular approach with supervised ML is to use a multilayer perceptron to detect troubled cells^{61–65}. An alternative to supervised ML is unsupervised ML, which involves algorithms that analyze data to identify patterns without relying on explicit labels or prior knowledge. These methods excel at uncovering hidden structures and relationships in complex datasets, making them valuable for tasks such as exploratory data analysis and anomaly detection. Examples of unsupervised ML techniques include k-means, Gaussian Mixture Model (GMM), and DBSCAN. These methods have demonstrated effectiveness in various applications, enabling researchers to gain insights and discover valuable information in the data without the need for labeled training examples. In the field of computational fluid dynamics (CFD), unsupervised ML models have been applied to tasks such as identifying flow regions within the flow field^{66,67} and performing mesh adaptation⁶⁸. However, the potential of unsupervised ML techniques to develop numerical schemes with shock-capturing capabilities remains largely unexplored.

This study focuses on the development of a novel shock-capturing sensor using unsupervised machine learning techniques. The sensor devised in this research demonstrates high accuracy by effectively identifying shocks, while other features such as turbulence or unresolved regions remain undetected. The shock capturing technique is coupled with an artificial viscosity approach and the DGSEM method^{69–71}, resulting in a precise and resilient discretization. A notable feature of this sensor is its parameter-free nature, which eliminates the need for manual adjustment. To assess its performance, a comprehensive comparison is conducted with state-of-the-art alternatives in the field.

This work is organized as follows: section II presents the Navier-Stokes equations, including the additional stabilization terms. Section III presents the methodology, explaining the new shock detection technique, and section IV describes the traditional sensors used as a reference. Section V summarizes the numerical approximation in space and time. Section VI

displays the results, comparing the new methodology with state-of-the-art alternatives. Finally, section VII concludes the study, outlining the findings and their implications.

II. NAVIER-STOKES EQUATIONS

The Navier-Stokes equations are a set of advection-diffusion equations on a spatial domain Ω for the conservative variables, $\mathbf{q} = (\rho, \rho\vec{v}, \rho e)^T$. These equations can be expressed using the notation presented in 72 as follows:

$$\begin{aligned} \mathbf{q}_t + \nabla \cdot \vec{\mathbf{f}}_e &= \nabla \cdot \vec{\mathbf{f}}_v, \\ \vec{\mathbf{f}} &= (\mathbf{f}, \mathbf{g}, \mathbf{h})^T, \quad \nabla \cdot \vec{\mathbf{f}} = \frac{\partial \mathbf{f}}{\partial x} + \frac{\partial \mathbf{g}}{\partial y} + \frac{\partial \mathbf{h}}{\partial z}, \end{aligned} \quad (1)$$

where ρ denotes the density, \vec{v} represents the velocity vector, and e corresponds to the specific total energy. Additional information on the advective and viscous fluxes, $\vec{\mathbf{f}}_e$ and $\vec{\mathbf{f}}_v$, can be found in appendix B 1.

In this study, we present a shock-capturing sensor and evaluate its effectiveness within the stabilization framework introduced by Guermond and Popov⁷³. The primary objective is to address the limited numerical dissipation of high-order schemes by introducing supplementary viscosity.

To achieve this, we incorporate an additional viscous term into eq. (1), such that $\vec{\mathbf{f}}_v \rightarrow \vec{\mathbf{f}}_v + \vec{\mathbf{f}}_a$. This augmentation allows us to compensate for the insufficient dissipation in the original formulation.

$$\begin{aligned} \vec{\mathbf{f}}_a &= \alpha_a \begin{pmatrix} \nabla \rho \\ \nabla \rho \otimes \vec{v} \\ \nabla (\rho e_i) + \frac{1}{2} |\vec{v}|^2 \nabla \rho \end{pmatrix} + \mu_a \begin{pmatrix} 0 \\ \rho \nabla^s \vec{v} \\ \rho \vec{v} \cdot \nabla^s \vec{v} \end{pmatrix}, \\ \nabla^s \vec{v} &= \frac{1}{2} \left(\nabla \vec{v} + (\nabla \vec{v})^T \right). \end{aligned} \quad (2)$$

The values of α_a and μ_a in eq. (2) govern the level of artificial dissipation, and we calculate them based on the value of a sensor $s \in [0, 1]$.

The specific relationship between the sensor, s , and the parameters α_a and μ_a is based on the spatial discretization employed. Typically, it requires scaling α_a and μ_a with an estimate of the sub-cell resolution to remove the dependence of viscosity on the element size. In this study, we adopt a standard scaling that assumes a spatial tessellation of the domain into

elements, as expressed by:

$$\alpha_a = \mu_a = \mu_0 \frac{V^{1/d}}{P+1} s. \quad (3)$$

Here, V denotes the volume of the element, d is the spatial dimension, and P is the polynomial order used to represent the solution within the element. More details on the numerical approach used to approximate the solution of eq. (1) are elaborated in section V and appendix B.

In the following section, we propose a novel method to compute the sensor value s . Other standard approaches are detailed in section IV.

III. UNSUPERVISED MACHINE LEARNING BASED SHOCK SENSOR

Clustering algorithms aim to identify patterns in the given feature space by grouping points based on shared properties. In the context of this study, our primary focus is on detecting regions of the flow that contain shocks. Shocks are identified by high gradients in the flow variables. However, these discontinuities typically occupy a relatively small portion of the fluid domain, resulting in only a small percentage of nodes being part of the identified clusters. Consequently, the majority of points in the feature space will tend to be concentrated around low values, while the clusters associated with discontinuities should be small and situated further into the higher-gradient region.

Among the various unsupervised machine learning algorithms available, we opt for the Gaussian Mixture Model (GMM) because of its advantages in our context. One of the key benefits is that it only requires one parameter, the number of clusters, and our implementation can handle it automatically, reducing the need for manual tuning. Furthermore, the GMM exhibits excellent efficiency in terms of implementation. The operations involved in iteratively updating the clusters can be expressed as reductions over threads and processes, leading to minimized communication between them. This efficient parallel performance ensures that the cost of detecting shocks does not significantly impact the scalability of the software. Given our ultimate goal of integrating this sensor into a stabilization approach for a Computational Fluid Dynamics solver, the favorable parallel performance of the GMM is crucial in maintaining the scalability of the software and overall performance.

A. Gaussian Mixture Model (GMM)

The GMM assumes that the points in the feature space have been randomly drawn from a combination of Gaussians, each with a certain probability, denoted τ , of being selected. The Probability Density Function (PDF) of the GMM is given by:

$$\begin{aligned}
 f(\vec{x}) &= \sum_{i=0}^K f_i(\vec{x}), \quad f_i(\vec{x}) = \tau_i N_v(\vec{x}; \vec{\mu}_i, \mathbf{S}_i), \\
 N_v(\vec{x}; \vec{\mu}, \mathbf{S}) &= \frac{1}{\sqrt{(2\pi)^v |\mathbf{S}|}} \exp\left[-(\vec{x} - \vec{\mu})^T \cdot \mathbf{S}^{-1} \cdot (\vec{x} - \vec{\mu})\right], \\
 \sum_{i=0}^K \tau_i &= 1,
 \end{aligned} \tag{4}$$

where v is the dimension of the feature space ($\vec{x}_i \in \mathbb{R}^v$), K is the number of components, and with expected values $\{\vec{\mu}_i\}_{i=0}^K$ and covariance matrices $\{\mathbf{S}_i\}_{i=0}^K$. The most common approach for fitting the mixture to the given points is the *Expectation-Maximization* (EM) algorithm. This iterative technique is used to find the optimal values of the set of parameters $(\tau_i, \vec{\mu}_i, \mathbf{S}_i)$ that maximizes the log-likelihood of the data,

$$\log L = \log \sum_{i=0}^K \sum_{j=0}^N \tau_i N_v(\vec{x}_j, \vec{\mu}_i, \mathbf{S}_i). \tag{5}$$

The GMM fitting process consists of two main steps: the E step and the M step. In the E step, each point is assigned probabilities of belonging to different clusters, calculated from $f_i(\vec{x})$ in eq. (4). The M step utilizes these probabilities to update the parameters that characterize the clusters, namely $(\tau_i, \vec{\mu}_i, \mathbf{S}_i)$. Below, we provide a sketch of the implementation used in our simulations in Algorithms 1 to 3.

In the main loop we have introduced an additional step to ensure that no two clusters overlap. In our implementation, clusters are considered to overlap when all components of the vector connecting their centroids have an absolute value lower than a certain tolerance (2×10^{-5} is used in this work). When such overlap occurs, we remove the second cluster and then readjust the parameters of the Gaussian mixture accordingly. This additional step proves to be particularly valuable during initial iterations, especially if the initial conditions are incompatible with the boundary conditions. In such cases, the presence of strong shocks and oscillations can potentially “confuse” the algorithm, leading to erroneous results or even causing the numerical scheme to diverge. The removal of overlapping clusters helps

Algorithm 1: EM method applied to the Gaussian Mixture Model (see also algorithms 2 and 3).

Input: $x, \vec{\tau}, \vec{\mu}, \vec{S}, max_iters, \epsilon, \delta$

Output: $\vec{\tau}, \vec{\mu}, \vec{S}$

Initialize $\vec{\tau}, \vec{\mu}, \vec{S}$

$prevlogL \leftarrow \infty$

for $iter$ in $1, \dots, max_iters$ **do**

$logL, prob \leftarrow Estep(x, \vec{\tau}, \vec{\mu}, \vec{S})$

$\vec{\tau}, \vec{\mu}, \vec{S} \leftarrow Mstep(x, \epsilon, prob, \vec{\tau}, \vec{\mu}, \vec{S})$

Adaptation step: delete overlapping clusters

if $(logL - prevlogL)/logL < \delta$ **then**

Leave the loop. The algorithm has converged

else

$prevlogL \leftarrow logL$

end

end

stabilize the algorithm in such scenarios, preventing unwanted issues in the early stages of the computation.

Additionally, within the main loop of our CFD solver, where algorithm 1 is used, we employ different initialization methods based on the state of the previous time step:

- If no previous time step information is available, we use the k-means initialization method explained in appendix A.
- If previous information is available for a cluster, we use it as a “warm start” for the initialization process.
- If the cluster was deleted in the previous time step, we initialize it with a random centroid and a spherical covariance matrix.

Although the simulations consistently converged to very similar results, initializing from the k-means method helped us achieve more reproducible results and draw more robust conclu-

Algorithm 2: E step of the Gaussian Mixture Model.

Input: $x, \vec{\tau}, \vec{\mu}, \vec{S}$
Output: $\log L, prob$

for j *in* $1, \dots, nclusters$ **do**
 for i *in* $1, \dots, npoints$ **do**
 $prob_{ij} \leftarrow \log N(x_i, \tau_j, \mu_j, S_j)$
 end
end

$\log L \leftarrow 0$

foreach row *in* $prob$ **do**
 $s \leftarrow \text{LogSumExp}(row)$
 $row \leftarrow \exp(row - s)$
 $\log L \leftarrow \log L + s$
end

Algorithm 3: M step of the Gaussian Mixture Model.

Input: $x, \epsilon, prob, \vec{\tau}, \vec{\mu}, \vec{S}$
Output: $\vec{\tau}, \vec{\mu}, \vec{S}$

for j *in* $1, \dots, nclusters$ **do**
 $nlocalpts \leftarrow \sum_i prob_{ij}$
 $\tau_j \leftarrow nlocalpts/npts$
 $\mu_j \leftarrow \sum_i x_i \cdot prob_{ij}/nlocalpts$
 $S_j \leftarrow \sum_i prob_{ij} \cdot (x_i - \mu_j) \otimes (x_i - \mu_j)/nlocalpts$
 $(S_j)_{ii} \leftarrow (S_j)_{ii} + \epsilon$
end

sions. This approach ensured greater stability in the initialization process and contributed to better consistency in the results obtained during the simulations.

B. Feature space

As mentioned above, shock waves are characterized by large gradients and oscillations. However, these features can also appear in other regions, such as turbulent and under-resolved areas. For this reason, it is essential to carefully consider the physics of the problem when choosing the gradients to define the feature space. By taking into account the specific characteristics of shock waves and distinguishing them from other phenomena, we can ensure a more accurate and reliable identification of shocks, while avoiding potential misclassifications in turbulent or under-resolved regions.

In this work we have considered:

- $(\nabla \cdot \vec{v})^2$,
- $\|\nabla p\|^2$,

mapped into the range $[0, 1]$ in both cases. In shocks, pressure gradients are notably large, whereas in most regions of the flow, including boundary layers and turbulence, they are limited to much lower values. Additionally, compressibility plays a significant role in supersonic features. To account for this effect, we include the divergence of the velocity in the feature space. For the sake of completeness, appendix C includes examples of alternative feature spaces.

C. Sensor definition

We aim to create the clustering sensor s_c from the GMM output, focusing on obtaining element-wise values from the nodal probabilities for comparison with other sensors in the literature.

We start by sorting the clusters based on the distance between their centroids and the origin. This straightforward implementation yields good results, as all variables considered in the feature space are positively correlated with the strength of the discontinuities.

The element-wise values of the sensor are calculated by determining the most likely cluster for each node and then selecting the highest identifier (corresponding to the furthest cluster from the origin), as shown in eq. (6):

$$s_c = \frac{1}{K} \arg \max_{k \in [0, K]} \left(\max_{\vec{x}_i \in e} f_k(\mathbf{u}(\vec{x}_i)) \right), \quad e \in \Omega. \quad (6)$$

It is important to note that the division by K scales the sensor to the range $s_c \in [0, 1]$, which is then used as s in eq. (3). This scaling ensures that the sensor values align appropriately with the requirements of eq. (3), where s is used to determine the viscosity parameters α_a and μ_a . While other possibilities, such as using averaged probabilities over the nodes of an element to determine its clustering, are also valid, eq. (6) adopts a more conservative approach. Detecting a single solution point is sufficient to label an entire element as problematic.

IV. TRADITIONAL SENSORS

A. Modal sensor of Persson and Peraire

A widely used sensor within the high-order community, denoted as s_m , relies on a modal representation of certain flow variables⁷⁴. In this approach, each mode is associated with a specific spatial frequency, and since higher frequencies correspond to larger gradients, the sensor estimates the smoothness of a scalar field u based on the relative weight of its highest-frequency modes in the approximation. The expression for the modal sensor is given as follows:

$$s'_m = \log \frac{\langle u_h, u_h \rangle}{\langle u, u \rangle}. \quad (7)$$

Here, u_h represents the highest frequency modes of u , i.e., all modes that include at least the highest mode in one of the directions. In our case, we use $u = p\rho$, and we also include tests with other variables (discussed in appendix C) to present a comprehensive evaluation of the performance of the sensor.

In section V A, we explain that the solver utilized to compute the results in this work implements a nodal formulation of the spatial discretization based on Lagrange polynomials. As a result, we first perform a basis change to express the variables of interest as a linear combination of Legendre polynomials. Both bases span the same polynomial subspace, facilitating the conversion between the two representations.

B. Integral sensor

Considering that discontinuities introduce large gradients in the solution, we adopt a simple sensor⁴⁵, denoted as s_a , which is based on the integral of a certain variable u inside each element. The expression for the sensor is given as follows:

$$s'_a = \frac{\sqrt{\langle u, u \rangle}}{V}. \quad (8)$$

In our results, we specifically use $u = \|\nabla p\|$, but we also include some tests with other potential choices in appendix C.

C. Sensor scaling

The sensors presented in sections IV A and IV B are not confined to the interval $[0, 1]$, unlike our proposed GMM sensor. To address this, we apply the scaling technique introduced by 74 to the raw sensor values:

$$s = \begin{cases} 0 & \text{if } s' < s_0 - \Delta s, \\ 1 + \sin \frac{\pi(s' - s_0)}{2\Delta s} & \text{if } s_0 - \Delta s \leq s' \leq s_0 + \Delta s, \\ 1 & \text{if } s' > s_0 + \Delta s. \end{cases} \quad (9)$$

The parameters s_0 and Δs serve as the center and width of the mapping from the original interval of s' to the final range $s \in [0, 1]$. This scaling ensures that all sensors, regardless of their original value range, are transformed to the interval $[0, 1]$, allowing meaningful and consistent comparisons between different sensor outputs.

V. NUMERICAL DISCRETIZATION: HORSES3D

The main objective of our research is to develop a sensor capable of detecting shock waves in both low- and high-order Navier-Stokes solvers and to utilize it for simulation stabilization. To achieve this, we integrate our sensor with the open-source software HORSES3D⁷¹.

By coupling our sensor with the artificial viscosity model represented by eqs. (2) and (3), we create a comprehensive computational setup. This allows us to assess the performance of the sensors in the context of a complete simulation framework. Such an integrated approach

provides valuable insights into the effectiveness and robustness of the sensor in detecting shock waves and stabilizing simulations across various scenarios.

A. Spatial discretization

In this study, we adopt a discontinuous Galerkin (DG) approach to discretize the spatial terms of eq. (1). Our physical domain is represented by a mesh of non-overlapping elements, and within each element, we approximate the values of various magnitudes using piecewise polynomials of order P . Since the solution is discontinuous, we introduce numerical fluxes to facilitate the transfer of information across neighboring elements. These fluxes serve as mathematical approximations to the Riemann problem generated at the discontinuities, ensuring that information is exchanged in a physically meaningful manner.

Our chosen approximation basis is tensor-product Lagrange polynomials, which means that the degrees of freedom in this scheme are simply the nodal values. Specifically, for the Navier-Stokes equations described in section II, each node is assigned a value of the state vector $\mathbf{q}_{ijk} = (\rho_{ijk}, \rho\vec{v}_{ijk}, \rho e_{ijk})^T$. The details of the mathematical derivation are provided in appendix B, which provides a comprehensive understanding of the formulation and implementation of our approach.

One of the most attractive features of the DGSEM is its ease of parallelization and high accuracy. This advantage led us to select sensor algorithms that preserve this property.

B. Temporal discretization

For temporal integration, we have chosen the well-known *Strong Stability Preserving Runge-Kutta* method, SSPRK33, proposed by Shu and Osher⁹. This three-stage Runge-Kutta method is of third order and is well-suited for our purposes. SSP schemes are convex combinations of forward Euler steps, which means that any property applicable to the simple forward Euler method will also hold for the higher-order SSP method. This means that it is possible to prove that the fully discretized scheme demonstrates entropy stability, i.e. the entropy of the flow can only decrease when there is a net flux through the boundaries of the domain. This stability is contingent on balancing the time derivative of the entropy with the dissipation introduced by the forward Euler method, which imposes a restriction on the

maximum allowable time step⁷⁵.

To further enhance the stability of the time integration without significantly reducing the time step size, we incorporate the positivity-preserving limiter developed by Zhang and Shu⁷⁶ at the end of every stage of the SSPRK33 integrator. The combination of artificial viscosity with this limiter has shown promising results in stabilization. On the one hand, the limiter can prevent negative values of density and pressure when a certain CFL condition is met; however, it does not eliminate oscillations from the solution. Additionally, it often requires excessively small time steps after several iterations. On the other hand, the artificial viscosity approach negatively impacts the viscous CFL number, resulting in the smearing of oscillations and the imposition of a smaller time step. By utilizing both methods together, we benefit from the additional dissipation provided by the artificial flux, which effectively eliminates oscillations, while the limiter allows for the use of larger time steps. This combined approach strikes a balance between stability and efficiency, resulting in a more robust and accurate simulation of the flow dynamics.

VI. RESULTS

In this section, we conduct a comparative analysis of our GMM sensor, as described in section III, with other well-known sensors outlined in section IV. The results presented herein are computed using the open-source software HORSES3D⁷¹ and are based on the discretization described in section V, along with the following key components.

Starting from a constant initial condition equal to the free stream flow, we employ the SSPRK33 method (detailed in section VB) with a time step of $\Delta t = 2 \times 10^{-4}$ for temporal discretization. Note that HORSES3D employs a non-dimensional formulation of the Navier-Stokes equations; therefore, the magnitudes given in this and the following sections are also non-dimensional. For the viscous terms, we utilize the BR1⁷⁷ scheme with entropy gradients, incorporating central numerical fluxes for gradients and viscous fluxes. To enhance the robustness of the simulations, we adopt the split-form of Chandrashekar⁷⁸ to discretize the advection term. The Riemann solver for inter-element fluxes is the two-point flux of Chandrashekar, complemented with additional dissipation from the matrix method presented in 78 and 79.

In all cases, we run the simulations for 3×10^5 iterations, resulting in a final time of $t_f = 60$,

considering the chosen Δt . To minimize the impact of the sensors on execution time, we perform a “sensor pass” once every ten iterations. This strategy maintains robustness while significantly reducing the computational cost of the stabilization process (see section VID for more details).

Although the tests are two-dimensional, the high Reynolds numbers involved ensure the appearance of turbulent regions. It is important to note that turbulence is inherently a three-dimensional phenomenon, and thus these two-dimensional regions do not fully capture the complete behavior of the flow. However, for the purpose of our study, these regions suffice, as they introduce gradients that must be differentiated from the ones representing shocks.

With this comprehensive setup, we proceed to compare the performance of our novel sensor against other established sensors, providing valuable insights into the effectiveness and reliability of our proposed approach in various scenarios.

A. Inviscid flow around a cylinder at Mach 3

The objective of this test is to evaluate the performance of the sensors in a purely hyperbolic scenario, where boundary layers are absent and large gradients consistently indicate the existence of discontinuities or regions of strong turbulence. We recreate the two-dimensional setup from 80, featuring a Mach 3 flow inside a planar channel encountering a cylindrical obstacle.

For the simulations, we employ a rectangular, unstructured mesh with boundaries $\vec{x} \in [-1.2, 6.8] \times [-2, 2]$, and place a cylinder of diameter one at the center, $\vec{x}_c = (0, 0)$. As illustrated in fig. 1, the domain is divided into 8,145 elements, with smaller sizes implemented near the cylinder and the wake region to improve resolution. The mesh was generated with GMSH v4.11, and second-order elements are used to properly describe the surface of the cylinder. Within each element, we approximate the solution using polynomials of order 4, resulting in a total of 203,625 degrees of freedom.

For the boundary conditions, we enforce slip-wall (symmetry) conditions at the top and bottom boundaries, as well as on the surface of the cylinder. On the right side, we implement an outflow condition, while an inflow condition at Mach 3 is applied on the left side.

The artificial viscosity is defined with a constant value of $\mu_0 = 0.1$. To compute the final viscosity, we scale it based on the sensor value and the mesh size, following eq. (3). This

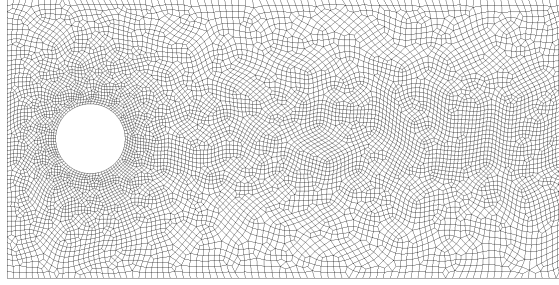


FIG. 1. Mesh used to compute the flow around a Mach 3 cylinder with no viscosity.

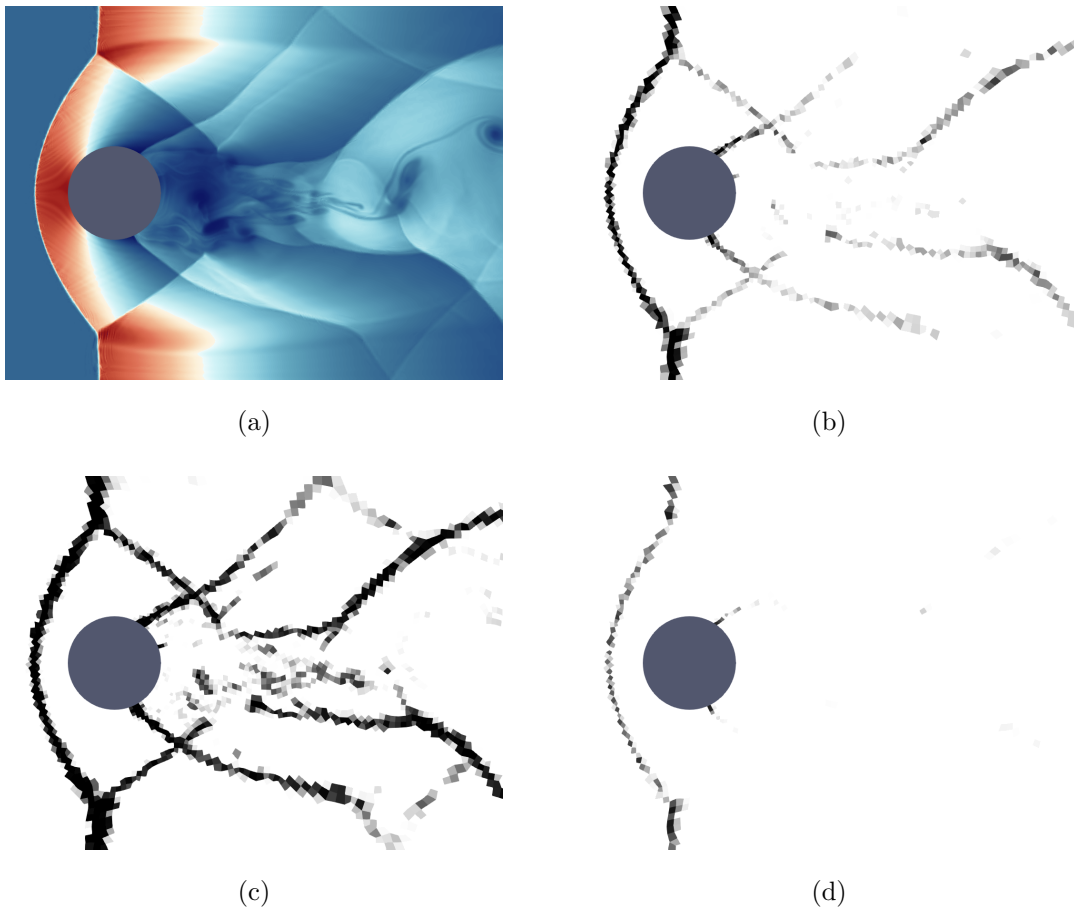


FIG. 2. Inviscid case after 300,000 iterations with the modal sensor of section IV A, using $p\rho$. a) density field, b) sensor with $s_0 = -2.5$ and $\Delta s = 1$. Sensor applied to the last iteration with $s_0 = -3.5$, $\Delta s = 1$ (c), and with $s_0 = -1.5$, $\Delta s = 1$ (d).

approach allows us to dynamically adjust the viscosity to account for regions with varying levels of discontinuities and turbulence.

All simulations exhibit similar overall behavior; however, slight differences in the artificial

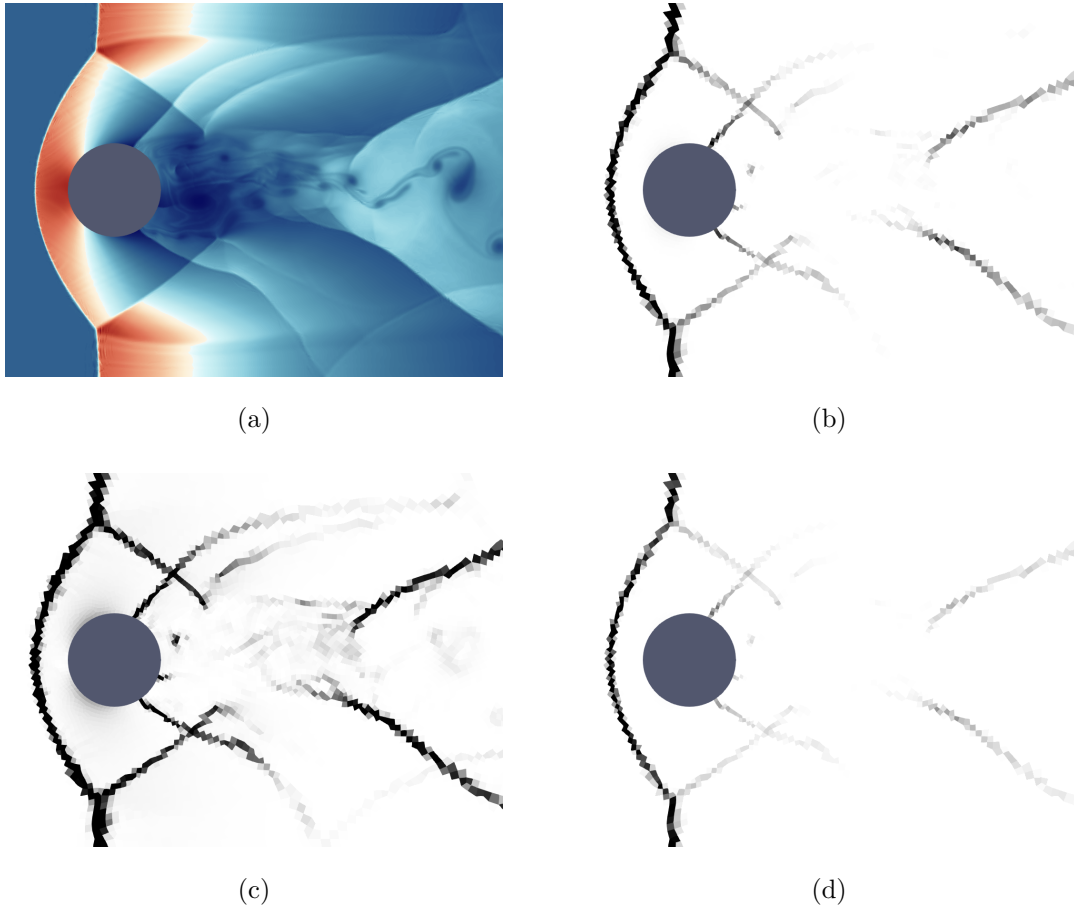


FIG. 3. Inviscid case after 300,000 iterations with the integral sensor of section IV B, using $\|\nabla p\|^2$. a) density field, b) sensor with $s_0 = 5.25$ and $\Delta s = 4.75$. Sensor applied to the last iteration with $s_0 = 2.5$, $\Delta s = 2.5$ (c), and with $s_0 = 8$, $\Delta s = 7$ (d).

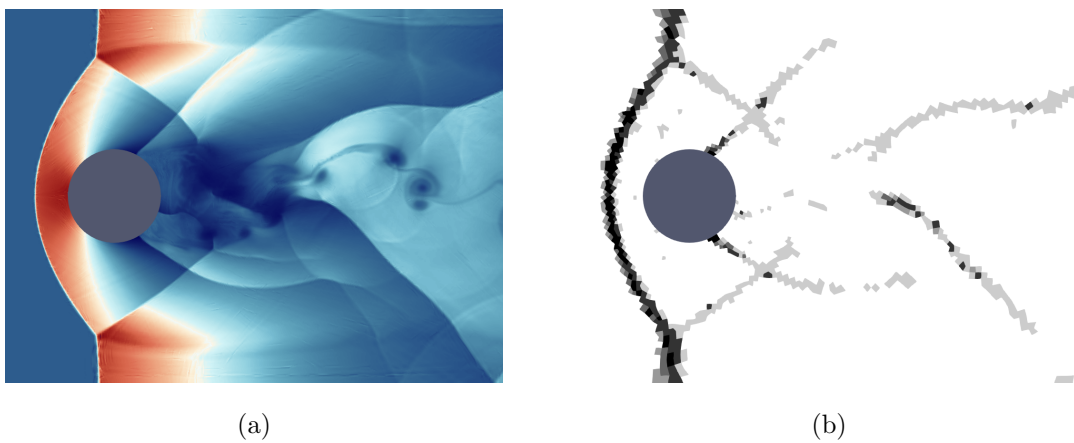


FIG. 4. Inviscid case after 300,000 iterations with our adaptive GMM sensor of section III, using $\|\nabla p\|^2, (\nabla \cdot \vec{v})^2$. a) density field, b) sensor with six clusters.

TABLE I. Parameters of the sensors for the inviscid cylinder.

Sensor	s_0	Δs	# of clusters
Modal	-2.5	1	-
Integral	5.25	4.75	-
GMM	-	-	6

viscosity among the different methods result in the triggering of turbulence in slightly distinct ways. As a consequence of the chaotic nature of turbulence, the instantaneous snapshots presented in figs. 2 to 4 show notable discrepancies in the wake region after $t = 60$. This phenomenon is well known, and it is why turbulence is typically evaluated in terms of averaged quantities.

However, in our case, the primary interest lies in effectively capturing shocks rather than analyzing these turbulent effects. Therefore, our figures showcase instantaneous snapshots that allow for a straightforward assessment of the performance of the sensor, particularly in terms of detecting and representing shocks in the flow field.

The three methods demonstrate good performance with the values specified in table I (sub-figures a and b), effectively disregarding almost the entire wake region and accurately detecting the main shock waves. In this scenario, the absence of a boundary layer around the cylinder delays the detachment point, causing the flow to accelerate until it reaches Mach numbers similar to those at the inlet. Subsequently, the flow experiences a sudden deceleration, eventually reaching a near-zero velocity just behind the cylinder.

The most challenging region of this test case is the strong shock that appears at the detachment point. This shock is responsible for the development of the wake downstream, where it interacts with the reflections of the main shock wave generated in front of the cylinder. Capturing and representing this region accurately is crucial to the overall fidelity of the simulation results.

Our novel GMM sensor performs exceptionally well in this test case. The automatic clustering capability of the GMM enables it to adapt to the feature space effectively. It can accurately detect regions of decreasing intensity near shocks while also correctly grouping all smooth regions into the same cluster. As a result, the sensor provides a smoother transition between detected and undetected regions, which is a crucial aspect in element-wise artificial

viscosity models since discontinuities in the viscosity field can introduce errors⁴⁰.

Furthermore, the sensor distribution obtained using the GMM-based algorithm shows excellent agreement with the distributions from the modal and integral sensors. This highlights a significant advantage of our method: it requires minimal parameter tuning since the algorithm is adaptive and regions are consistently and accurately identified without the need for fine-tuning.

The only parameter that needs to be introduced is the number of clusters, and its impact is minimal since the algorithm automatically adjusts to the data distribution. Having more clusters results in smoother transitions between smooth and non-smooth regions, but the sensor remains effective with a relatively small number of clusters. We examine this statement in section VI C, demonstrating that dissipation is only added where necessary across a wide range of cluster numbers.

To illustrate the importance of finding appropriate values for the sensor thresholds, we modify the parameter s_0 and Δs of eq. (9) as shown in the c and d sub-figures of figs. 2 and 3. This emphasizes the need to carefully select sensor thresholds to ensure accurate identification and representation of shocks and other flow features.

B. Viscous flow around a cylinder at Mach 2

This test introduces several characteristics of real flows, making it more complex than the previous case. In the previous test, viscosity was only included in shocks, which was shown to be critical for stabilizing under-resolved features and obtaining a robust scheme. However, in this case, the flow is viscous everywhere, with a Reynolds number of 10^5 based on the diameter of the cylinder.

The main objective of this test is to assess the performance of our sensor in simulations with boundary layers, as their proper representation is crucial for the overall stability of the discretization. While shock sensors are designed to detect discontinuities, they may also identify other under-resolved regions of the flow. In the context of turbulent flows, this may lead to a failure to match the real energy spectrum. However, for boundary layers, the challenge lies in maintaining robustness in the numerical solution.

Elements in boundary layers are typically stretched significantly to resolve normal gradients while minimizing the number of degrees of freedom. However, this approach impacts

negatively the maximum allowed time step, which is already small in high-order schemes with explicit time integration. The introduction of artificial viscosity into these elements worsens the situation, resulting in even shorter time steps.

In this test case, we aim to examine how our sensor performs in the presence of boundary layers and ensure that it effectively identifies and treats under-resolved regions while maintaining the overall stability and accuracy of the simulation.

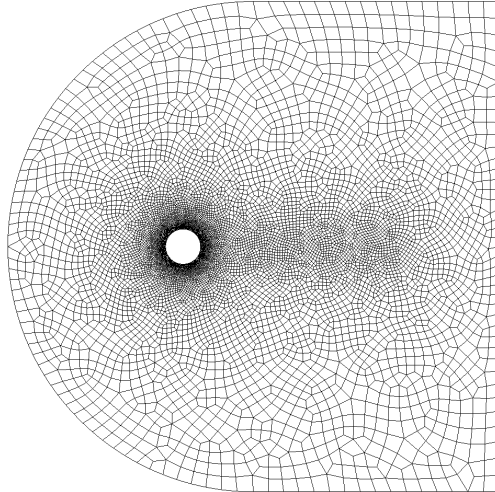


FIG. 5. Mesh used to compute the flow around a Mach 2 cylinder at $Re = 100,000$.

The mesh, as shown in fig. 5, represents a free flow at Mach 2 with a cylinder placed at the origin with a diameter of one. The unstructured mesh has bounds $x \in [-5, 9]$ and $y \in [-7, 7]$, and was generated using GMSH v4.11. It comprises 9,713 elements of second order, concentrated around the cylinder and in the wake region. The polynomial approximation used is of order four, resulting in a total of 242,825 degrees of freedom.

We apply inflow boundary conditions on the semicircular left side of the mesh and outflow boundary conditions on the top, right, and bottom sides. The surface of the cylinder is modeled with a no-slip boundary condition. Since the flow is viscous in this case, we found that a viscous constant $\mu_0 = 0.08$ for eq. (3) provides the best results.

This test case models a more realistic configuration, allowing for quantitative comparisons with results from the literature. It has been extensively studied both experimentally and numerically in 81–83, and we have obtained satisfactory results for the pressure distribution around the cylinder surface, as shown in fig. 6.

The simulations were carried out using the sensors specified in table II. While it is coin-

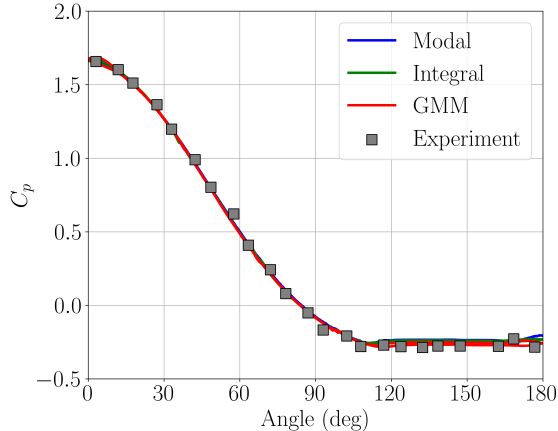


FIG. 6. Pressure coefficient around the cylinder averaged over 20 time units. The experimental data was obtained in 81. The angle is measured from the stagnation point, i.e. the left-most position of the surface of the cylinder.

cidental that the parameter values match those of table I, we invite the reader to refer to appendix C for additional examples in which the values differ. In any case, the C_p distribution shown in fig. 6—averaged over 10^5 time steps or 20 time units—closely matches the experimental data from 81 with the three sensors. The detachment point, at an angle of approximately $\theta_s \simeq 110^\circ$, is also well captured, consistent with 81–83. This angle is measured from the stagnation point and, since the case is symmetric, has the same sign on both sides of the cylinder.

TABLE II. Parameters of the sensors for the viscous cylinder.

Sensor	s_0	Δs	# of clusters
Modal	-2.5	1	-
Integral	5.25	4.75	-
GMM	-	-	6

Before the detachment point, the pressure gradient across the boundary layer is smooth, allowing for an accurate approximation of the pressure distribution. However, in the wake region, a recirculation bubble forms, and the pressure field is not captured with the same accuracy. It is also important to note that we do not expect a perfect match, as the mesh is not specifically optimized to capture all the scales involved in the boundary layer. The y^+

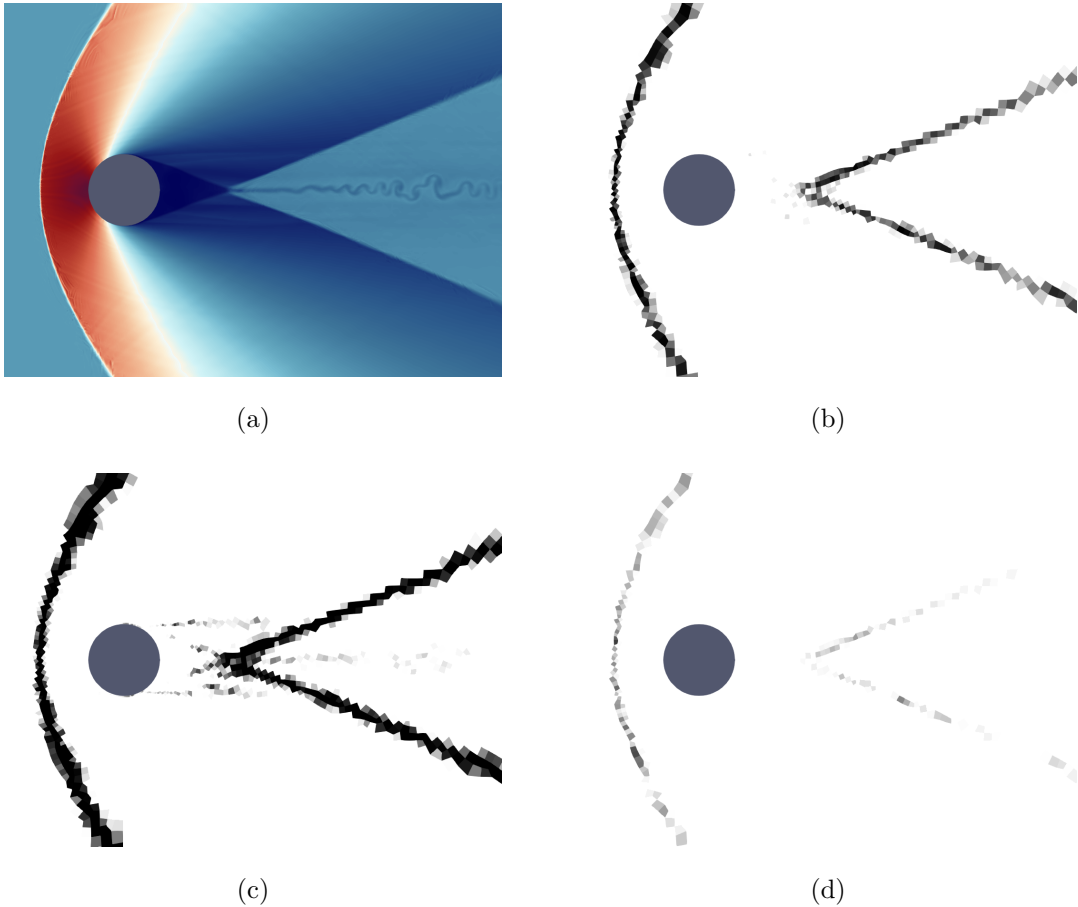


FIG. 7. Viscous case after 300,000 iterations with the modal sensor of section IV A, using $p\rho$. a) density field, b) sensor with $s_0 = -2.5$ and $\Delta s = 1$. Sensor applied to the last iteration with $s_0 = -3.5$, $\Delta s = 1$ (c), and with $s_0 = -1.5$, $\Delta s = 1$ (d).

value of our discretization is around 20, indicating that the element size and distribution of high-order nodes are not fine enough to accurately resolve the viscous stresses close to the wall. As a result, we were unable to accurately compare the total drag with the experimental data, but our pressure distribution results remain accurate and in good agreement with the experiments.

In figs. 7 to 9 (sub-plots a and b), we present the density plots and sensor distributions for the three methods. All three approaches successfully capture the main shock wave with sub-cell resolution, and the oscillations in the wake region are not dissipated.

Upon analysis of the sensor values, we observe that no additional viscosity is introduced in the smooth regions or in the wake downstream. This lack of additional viscosity explains the high level of detail observed in the results, such as the accurate representation of detachment

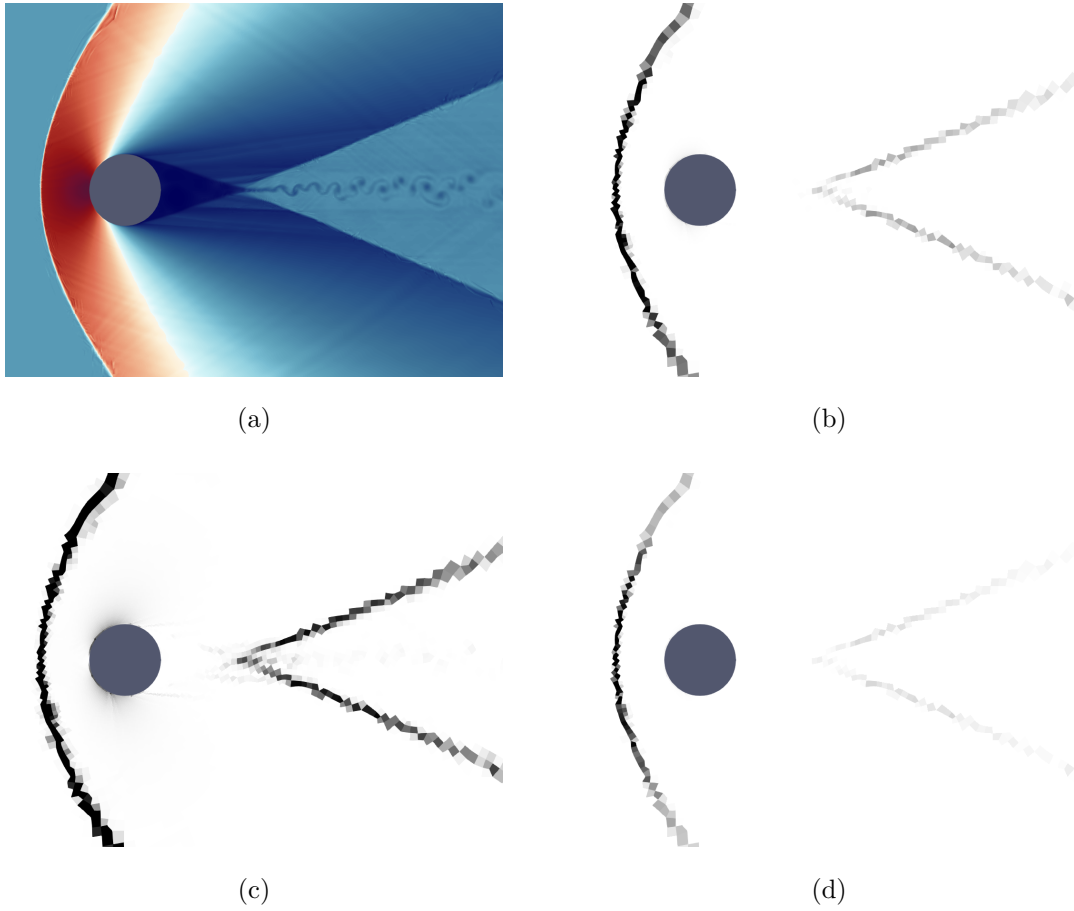


FIG. 8. Viscous case after 300,000 iterations with the integral sensor of section IV B, using $\|\nabla p\|^2$. a) density field, b) sensor with $s_0 = 5.25$ and $\Delta s = 4.75$. Sensor applied to the last iteration with $s_0 = 2.5$, $\Delta s = 2.5$ (c), and with $s_0 = 8$, $\Delta s = 7$ (d).

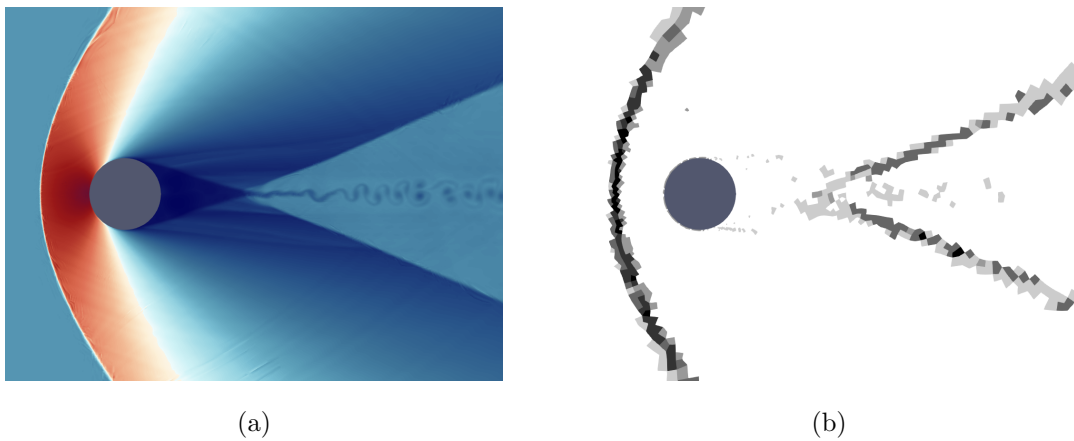


FIG. 9. Viscous case after 300,000 iterations with our adaptive GMM sensor of section III, using $\|\nabla p\|^2, (\nabla \cdot \vec{v})^2$. a) density field, b) sensor with six clusters.

shocks, small vortices in the wake, or thin shock waves.

As expected, the sensors perform well in capturing the shock waves in this test case, given their successful performance in the inviscid scenario. However, the main challenge in this setup lies in not detecting the boundary layer around the cylinder.

Boundary layers and shock waves are physically distinct phenomena, but they both impose significant computational demands and can induce oscillations and non-physical behaviors in high-order approximations. In our DGSEM, no-slip boundary conditions are imposed weakly, which means that the discontinuity between the flow near the boundary and the actual boundary condition can grow if the approximation is excessively coarse. This phenomenon is particularly evident in supersonic simulations with transient flow configurations, leading to high numerical fluxes that introduce oscillations in the boundary layer. At this stage, even a small addition of artificial viscosity can lead to a simulation crash.

Taking into account this, it is evident that the modal and integral sensors in figs. 7 and 8 needed precise threshold selection to avoid incorrect detection patterns, as deviations from these values resulted in inaccuracies (see sub-figures c and d). In contrast, our GMM sensor does not suffer from this limitation, as the clustering process is automatic, and the discrimination between smooth and non-smooth regions remains independent of the number of clusters used. Numerical evidence supporting this is presented in section VI C.

C. Analysis of the feature space and sensitivity to the number of clusters

The preceding test cases have served as a qualitative assessment of our GMM-based sensor, particularly when compared to other established sensors in the literature. In this section, our objective is to provide a clearer understanding of how the number of clusters affects the properties of the sensors.

A common metric used to assess the goodness of fit of a model to the given data is the Bayesian Information Criterion (BIC), defined as

$$\text{BIC} = -2 \log L + N_p \log N,$$

where $\log L$ is the logarithm of the likelihood, N_p is the number of free parameters of the model, and N is the number of points in the feature space. For the Gaussian Mixture Model

(GMM), the number of free parameters is given by

$$N_p = K + Kv + K \frac{v(v+1)}{2} - 1,$$

using the definitions of eq. (4), and $\log L$ takes the form of eq. (5). Another well-known metric is the Akaike Information Criterion (AIC), defined as

$$\text{AIC} = -2 \log L + 2N_p.$$

The difference between these two criteria is $N_p(2 - \log N)$, and in our case, it is several orders of magnitude smaller than the log-likelihood. As both methods would yield the same conclusions, we continue with the BIC in the following discussion.

We begin by extracting the solution of the viscous flow case at $t = 60$ obtained using the GMM sensor, as depicted in fig. 9. Using a Python code and the scikit-learn library⁸⁴, we compute the Bayesian Information Criterion (BIC) for a varying number of clusters, ranging from one to six.

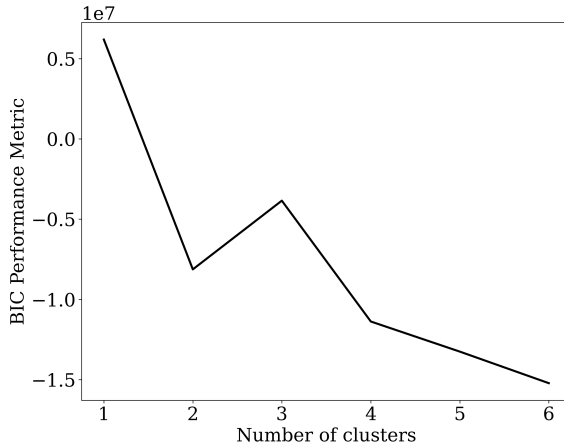


FIG. 10. Bayesian information criterion as a function of the number of clusters.

The plot in fig. 10 clearly demonstrates that the use of two clusters is sufficient to capture most of the information, since the rate of descent in the BIC decreases significantly after this point. This rule-of-thumb is often referred to as the “elbow method”, and takes into account that the BIC balances lower values of the log-likelihood with higher numbers of parameters to avoid favoring overfitted models. In this specific application of the GMM for a shock-capturing sensor, we have found that increasing the number of clusters beyond two

does not negatively impact the performance of the artificial viscosity approach used in this work.

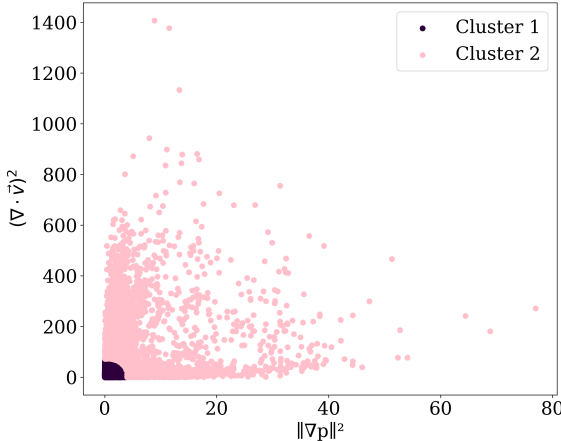


FIG. 11. GMM sensor with two clusters applied to the viscous case.

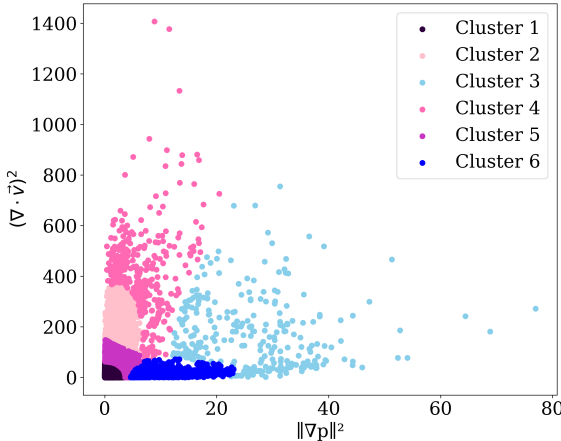


FIG. 12. GMM sensor with six clusters applied to the viscous case.

The Gaussian mixture models with one to six clusters effectively differentiate the two main regions: smooth flow and discontinuities. As shown in fig. 11, cluster 1 encompasses the vast majority of points representing smooth regions, while cluster 2 includes the fewer nodes associated with shock waves. Both the BIC and the feature-space plot support the idea that this division of the feature space is the most representative of the dataset. Therefore, when applying the GMM shock sensor to a specific numerical discretization, using two clusters as a default value is likely to yield reliable and accurate results. However, as we have

explained, the artificial viscosity method we have used in this work benefits from smooth spatial transitions in the viscosity field. Therefore, using only two clusters might not be optimal.

In fig. 12, we present the feature space and the groups made by the GMM when using six clusters. It is evident that the first cluster has an almost identical shape, indicating that the differences between this cluster and the others are significant enough to ensure a clear distinction between smooth and non-smooth regions. Consequently, we can add more levels to the sensor by increasing the number of clusters. In our simulations, we could not exceed ten clusters because the adaption step we introduced caused some clusters to collapse. The ideal number of clusters might depend on the specific case being simulated, particularly on the ratio of nodes in discontinuous regions compared to nodes in smooth regions. However, this issue does not significantly impact our discussion, as our primary goal is to describe a sensor algorithm capable of detecting shock waves with a certain level of refinement. Based on our experience, using four to six clusters provides the best results.

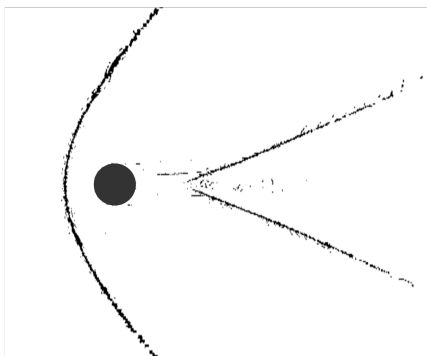


FIG. 13. Node-wise resolution of our proposed GMM sensor with two clusters.

Furthermore, our proposed GMM sensor has another advantage over the modal and integral sensors explained in sections IV A and IV B. By feeding the GMM with nodal values, the clusters that we obtain are also node-wise. While many traditional sensors, including the ones we have presented in this work, only provide a classification at the element level, our

GMM sensor can offer more specific information, enabling the use of sub-cell stabilization methods.

D. Performance scaling

In this section, we shift our focus to investigate the computational cost of our sensor. While it offers improved robustness in the numerical discretization, there is a trade-off in terms of increased computational requirements. To assess the performance of the GMM sensor, we performed a strong scaling test, comparing its efficiency with different parallelization strategies available in HORSES3D.

This software offers the advantage of parallelization in terms of both threads (OpenMP) and processes (MPI). In our testing, we evaluated the performance of the sensor under different combinations of parallelization methods. The results are presented in fig. 14, which

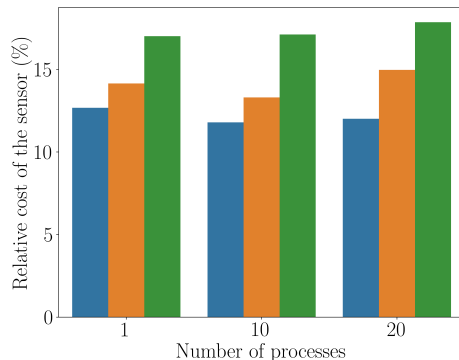


FIG. 14. Cost of evaluating the sensor relative to the total time of one time step in the case of the viscous cylinder. The measurements are performed over 20 time steps. Blue: 1 thread, orange: 2 threads, green: 4 threads.

illustrates the relative computational cost of the GMM-based sensor within a single time step. To generate these data, we used the solution obtained from the GMM-based sensor in section VIB (see fig. 9) and computed the metric for 20 iterations. The sensor computation time was then divided by the total time taken for the same 20 time steps.

Interestingly, we observed that the cost of the sensor does not vary with the number of processes used. This observation aligns with our explanation in section III, where we discussed that data transfer between processes is not a significant issue with the GMM

sensor. Since only small amounts of information need to be exchanged, the performance remains consistent regardless of the number of processes employed.

However, we did observe that the multithreaded performance of our implementation could be further optimized. The other operations performed by the software during a single time step scale better when increasing the number of threads. Consequently, there is a performance hit of around 10% to 20% when computing the sensor every time step. This effectively results in an overhead of 2% maximum in the total simulation time if the sensor is updated every 10 iterations. We justify this by recalling that we use an explicit time integration scheme (as described in section VB) and this typically involves small time-step sizes. Therefore, the solution undergoes minimal changes after a few time steps, and the sensor output remains virtually constant. The cost of the other traditional sensors considered in this work is at least an order of magnitude lower, but the impact is nevertheless low in all the cases, and the advantages of our proposed sensor offset this overhead.

Lastly, it is essential to emphasize that fig. 14 does not provide insight into the scalability of HORSES3D. Instead, it solely compares the performance of the new GMM-based sensor against the rest of the code. The constant cost observed with varying processes merely indicates that the GMM-based sensor scales well within the solver.

VII. CONCLUSIONS

In this article, we have introduced a shock detection algorithm based on Gaussian Mixture Models (GMMs) and integrated it into an existing high-order Computational Fluid Dynamics (CFD) solver. Unlike many common sensors, our method requires only one parameter, the maximum number of clusters, and provides default values that yield satisfactory results in most cases. The adaptive nature of the algorithm allows it to modify this parameter if the user-provided value is not suitable for the simulation, making it easy to use and apply.

The Bayesian formulation of our sensor allows it to leverage previous information, resulting in improved accuracy and performance. This feature makes it suitable for integration into the workflow of PDE solvers. We have successfully incorporated it into our open-source solver HORSES3D⁷¹ as part of a stabilization strategy based on element-wise artificial viscosity. The algorithm has demonstrated its effectiveness in challenging cases, including Mach 3 flows at moderately high Reynolds numbers. Although we have presented a simple

approach in this article, it has proven to be effective in enhancing the robustness of existing software.

We recognize that there is potential for further improvement and refinement of our approach. For example, we can exploit the node-wise nature of the algorithm to couple it with more accurate stabilization methods. Additionally, Bayesian inference techniques could be utilized to implement better prediction models for the number of clusters in the GMM. Exploring different feature spaces might also yield more suitable choices for shock detection. Although we have conducted various tests with different variables, a more comprehensive study of the influence of the feature space dimension and variable selection is left for future work.

Our research findings indicate that unsupervised machine learning methods hold promise in improving the performance of complex CFD codes. Such codes often encounter varied and complex geometries and flow configurations, which can be challenging to handle using traditional supervised algorithms that rely on training datasets. On the contrary, unsupervised methods, such as GMM-based shock detection, can adapt to diverse scenarios and offer robust solutions without the need for extensive training data. As the field of machine learning advances, we envision even greater opportunities to enhance CFD simulations and address real-world cases.

ACKNOWLEDGMENTS

Andrés Mateo has received funding from Universidad Politécnica de Madrid under the Programa Propio PhD programme. Kenza Tlaes was supported by Grant 080 Bis/PG/Espagne/2020 2021 of Ministère de l'Enseignement Supérieur et de la Recherche Scientifique, République Algérienne Démocratique et Populaires. Gonzalo Rubio and Eusebio Valero acknowledge the funding received by the Grant NextSim / AEI /10.13039/501100011033 and H2020, GA-956104. Esteban Ferrer would like to thank the support of Agencia Estatal de Investigación (for the grant "Europa Excelencia 2022" Proyecto EUR2022-134041/AEI/10.13039/501100011033) y del Mecanismo de Recuperación y Resiliencia de la Unión Europea, and the Comunidad de Madrid and Universidad Politécnica de Madrid for the Young Investigators award: APOYO-JOVENES-21-53NYUB-19-RRX1A0. Finally, all authors gratefully acknowledge Universidad Politécnica de Madrid (www.upm.es) for providing computing resources on

Magerit Supercomputer.

AUTHOR DECLARATIONS

Conflict of interest

The authors have no conflicts to disclose.

Author contributions

Andrés Mateo-Gabín: Conceptualization; Data curation; Methodology; Software; Visualization; Writing – original draft. **Kenza Tlaes:** Data curation; Formal analysis; Software; Visualization. **Eusebio Valero:** Conceptualization; Funding acquisition; Project administration. **Esteban Ferrer:** Conceptualization; Funding acquisition; Methodology; Project administration. **Gonzalo Rubio:** Conceptualization; Funding acquisition; Methodology; Supervision; Writing – review & editing.

DATA AVAILABILITY STATEMENT

The data that support the findings of this study are openly available in https://github.com/Andres-MG/2023_gmm_shock_sensor.

Appendix A: K-means clustering

The k-means algorithm defines clusters based on their centroids, and nodes are assigned to the closest ones. It produces hyperspherical clusters, making it suitable for feature spaces where the different groups are well defined and quasi-isotropic. The number of clusters is fixed at the beginning of the algorithm, and the final distribution is found iteratively, usually converging after a few steps (see algorithm 4). As an iterative method, it is necessary to have an initial state to begin the iterations. Therefore, if no information is available, we start the algorithm with a random distribution of clusters. However, if there is known data, we restart the algorithm from that starting point. In our work, this is the case when we use it to enhance the results of an unconverged GMM pass.

Algorithm 4: K-means.

Input: $nclusters, maxiters, x$ **Output:** $\bar{x}, clusters$ Initialize \bar{x} $clusters \leftarrow GetClusters(x, \bar{x})$ $prevclusters \leftarrow clusters$ **for** i in $1, \dots, maxiters$ **do** $\bar{x} \leftarrow GetCentroids(x, clusters)$ $clusters \leftarrow GetClusters(x, \bar{x})$ **if** $clusters = prevclusters$ **then**

Leave the loop. The algorithm has converged

else $prevclusters \leftarrow clusters$ **end****end**

The implementation is similar to the one described for the GMM in section III, and two steps are performed at each iteration. First, the centroids of the clusters are computed as the average position of all the points assigned to each group in the last iteration. Then, this new cluster distribution is used to recompute the distances between nodes and centroids, regrouping the points with the new definitions. The algorithm stops when the centroids are not updated in two consecutive iterations.

Appendix B: Details on the numerical formulation**1. Navier-Stokes equations**

Equation (1) states the generic form of an advection-diffusion equation, but does not introduce the specific form of the various terms. The advective, $\vec{\mathbf{f}}_e$, and viscous, $\vec{\mathbf{f}}_v$, fluxes

of the Navier-Stokes equations, are defined as

$$\begin{aligned} \mathbf{f}_e &= \begin{pmatrix} \rho u \\ \rho u^2 + p \\ \rho uv \\ \rho uw \\ \rho hu \end{pmatrix}, & \mathbf{f}_v &= \begin{pmatrix} 0 \\ \tau_{11} \\ \tau_{21} \\ \tau_{31} \\ \vec{\tau}_1 \cdot \vec{v} + q_1 \end{pmatrix}, \\ \mathbf{g}_e &= \begin{pmatrix} \rho v \\ \rho uv \\ \rho v^2 + p \\ \rho vw \\ \rho hv \end{pmatrix}, & \mathbf{g}_v &= \begin{pmatrix} 0 \\ \tau_{12} \\ \tau_{22} \\ \tau_{32} \\ \vec{\tau}_2 \cdot \vec{v} + q_2 \end{pmatrix}, \\ \mathbf{h}_e &= \begin{pmatrix} \rho w \\ \rho uw \\ \rho vw \\ \rho w^2 + p \\ \rho hw \end{pmatrix}, & \mathbf{h}_v &= \begin{pmatrix} 0 \\ \tau_{13} \\ \tau_{23} \\ \tau_{33} \\ \vec{\tau}_3 \cdot \vec{v} + q_3 \end{pmatrix}. \end{aligned}$$

These variables are related by the expressions

$$\rho e = \rho e_i + \frac{1}{2} \rho |\vec{v}|^2, \quad e_i = \frac{p/\rho}{\gamma - 1}, \quad p = \rho RT,$$

and the viscous flux is defined in terms of the stress tensor and the heat flux,

$$\begin{aligned} \tau_{ij} &= \mu \left(\frac{\partial v_i}{\partial x_j} + \frac{\partial v_j}{\partial x_i} - \frac{2}{3} \nabla \cdot \vec{v} \delta_{ij} \right), & \vec{\tau}_i &= (\tau_{1i}, \tau_{2i}, \tau_{3i}), \\ \vec{q} &= \kappa \nabla T, & \kappa &= \theta \mu R, \quad \theta = \frac{\gamma}{(\gamma - 1) \text{Pr}}. \end{aligned}$$

The Prandtl number, Pr , is characteristic of the medium, and we use a value of 0.72 for the air.

These definitions include conservation laws for the mass, momentum and energy, but not the entropy. However, it is also an important physical principle that the entropy of a closed system cannot decrease. To ensure that our numerical approximations also accommodate this law, we introduce the concept of mathematical entropy, S . This entropy is defined as a scaled version of the physical entropy, s ,

$$S = -\frac{\rho s}{\gamma - 1}, \quad s = \ln p - \gamma \ln \rho.$$

The derivative of this entropy function with respect to the conservative variables, \mathbf{q} , is a new set of variables called *entropy variables*, \mathbf{w} ,

$$\mathbf{w} = \nabla_{\mathbf{q}} S = \left(\frac{\gamma - s}{\gamma - 1} - \frac{\rho |\vec{v}|^2}{2p}, \frac{\rho u}{p}, \frac{\rho v}{p}, \frac{\rho w}{p}, -\frac{\rho}{p} \right)^T.$$

We use these entropy variables to compute the artificial viscosity flux of eq. (2), ensuring that the discretization is entropy-stable.^{45,73}

2. Spatial discretization

In this work, we follow a discontinuous Galerkin (DG) approach to discretize the spatial part of eq. (1). First, the physical domain is tessellated into non-overlapping elements, and each of them is mapped to the so-called standard element, E , defined as $\vec{\xi} \in [-1, 1]^3$. For each element, e , the mapping $\vec{x} = \vec{X}(\vec{\xi})$ relates the local coordinates in the reference element, $\vec{\xi} = (\xi, \eta, \zeta)^T \in E$, to the physical space, $\vec{x} = (x, y, z)^T \in e$, and allows the definition of eq. (1) in terms of operators defined in the reference element. From this mapping we can compute the local reference frame (covariant, \vec{a}_i , and contravariant, \vec{a}^i) in each element and the Jacobian, that gives an idea of the deformation of the element with respect to the standard space,

$$\vec{a}_i = \frac{\partial \vec{X}}{\partial \xi_i}, \quad \mathcal{J} \vec{a}^i = \vec{a}_j \times \vec{a}_k, \quad \mathcal{J} = \mathcal{J} \vec{a}^i \cdot \vec{a}_i.$$

Defining the matrices \mathbf{M} with columns $\vec{M}_i = \mathcal{J} \vec{a}^i$, and $\mathcal{M} = \mathbf{M} \otimes \underline{I}_5$ (\underline{I}_5 is the 5×5 identity matrix), state and block vectors can be easily projected from the covariant to the contravariant basis. In the case of gradients,

$$\begin{aligned} \mathcal{J} \nabla f &= \mathbf{M} \nabla_{\vec{\xi}} f, & \mathcal{J} \nabla \cdot \vec{f} &= \nabla_{\vec{\xi}} \cdot (\mathbf{M}^T \vec{f}) = \nabla_{\vec{\xi}} \cdot \vec{f}, \\ \mathcal{J} \nabla \mathbf{f} &= \mathcal{M} \nabla_{\vec{\xi}} \mathbf{f}, & \mathcal{J} \nabla \cdot \vec{\mathbf{f}} &= \nabla_{\vec{\xi}} \cdot (\mathcal{M}^T \vec{\mathbf{f}}) = \nabla_{\vec{\xi}} \cdot \vec{\mathbf{f}}, \end{aligned}$$

where \vec{f} and $\vec{\mathbf{f}}$ are the projections into the contravariant basis of a state and a block vector, respectively.

The weak form of eq. (1) is obtained in several steps. First, to avoid computing second derivatives, the gradients of the entropy variables, \mathbf{w} , are computed in a separate equation, $\vec{\mathbf{g}} = \nabla \mathbf{w}$. Then, the combination of eq. (1) with this definition of the gradients is multiplied by two test functions, ϕ and $\vec{\psi}$, and integrated over the reference element. After

application of the chain rule, we obtain the weak form that needs to be solved for each of the elements in the entire domain, Ω ,

$$\begin{aligned} \langle \mathcal{J}\mathbf{q}_t, \phi \rangle_E + \int_{\partial E} \phi^T \vec{\mathbf{f}}_e \cdot \hat{n} \, d\hat{S} - \langle \vec{\mathbf{f}}_e, \nabla_{\vec{\xi}} \phi \rangle_E &= \int_{\partial E} \phi^T (\vec{\mathbf{f}}_v + \vec{\mathbf{f}}_a) \cdot \hat{n} \, d\hat{S} - \langle \vec{\mathbf{f}}_v + \vec{\mathbf{f}}_a, \nabla_{\vec{\xi}} \phi \rangle_E, \\ \langle \mathcal{J}\vec{\mathbf{g}}, \vec{\psi} \rangle_E &= \int_{\partial E} \mathbf{w}^T \vec{\psi} \cdot \hat{n} \, d\hat{S} - \langle \mathbf{w}, \nabla_{\vec{\xi}} \vec{\psi} \rangle_E. \end{aligned} \quad (\text{B1})$$

In eq. (B1), \hat{n} and $d\hat{S}$ are the unit normal vector and the surface differential of the six planar faces of E (e.g. for the faces $\xi = \pm 1$, $\hat{n} = (\pm 1, 0, 0)^T$ and $d\hat{S} = d\eta d\zeta$). Since in a DG scheme there are no continuity constraints between the elements, these are used to exchange information between contiguous elements by solving the Riemann problem that they define. Therefore, we introduce so-called *numerical fluxes*, $\mathbf{f}^*(\mathbf{q}_l, \mathbf{q}_r, \hat{n})$, in the interfaces of the elements to approximate these one-dimensional Riemann problems.

The next step is introducing polynomial approximations of order P . Since we employ a *Discontinuous Galerkin Spectral Element Method* (DGSEM), the polynomial basis comprises the Lagrange polynomials, $\{l_i(x)\}_{i=0}^P$, associated to a set of nodes defined in the reference element. For example, the approximation of \mathbf{q} in a three-dimensional case for an element of the tessellation is

$$\begin{aligned} \mathbf{q} &\approx \mathbf{Q} = \sum_{i,j,k=0}^P \mathbf{Q}_{ijk} l_i(\xi) l_j(\eta) l_k(\zeta), \\ \mathbf{Q}_{ijk} &= \mathbf{q}(\xi_i, \eta_j, \zeta_k), \end{aligned}$$

and in the following we use uppercase letters for discretized variables. We also approximate the integrals with Gauss-Lobatto quadratures, using the nodes of the quadrature as interpolation points. In two and three dimensions, the interpolation nodes are defined as a tensor-product extension of the one-dimensional case.

To further increase the robustness of the discretization, we consider split-form derivative operators to reduce the adverse effects of aliasing. In the simple case of $f = ab$, its split-form derivative would be

$$\frac{\partial f}{\partial x} = \alpha \frac{\partial(ab)}{\partial x} + (1 - \alpha) \left(b \frac{\partial a}{\partial x} + a \frac{\partial b}{\partial x} \right), \quad (\text{B2})$$

for some value of α . It can be proved⁸⁵ that the derivative operator of the DGSEM can be used to define the discretized form of this split-form operators. Using a two-point flux, $F_{ij}^\# =$

$F^\#(Q_i, Q_j)$, that connects all the nodes in the direction of the derivative,

$$\frac{\partial f}{\partial x} \Big|_{x=\xi_i} \approx \sum_{j=0}^P D_{ij} F_j = \sum_{j=0}^P 2D_{ij} F_{ij}^\#.$$

The application of all these previous concepts into eq. (B1) yields the expression of the time derivative for each degree of freedom:

$$\begin{aligned} \mathcal{J}_{ijk} \mathbf{Q}_{t,ijk} + \mathbb{D}_{ijk}^\# \left(\overset{\leftrightarrow}{\mathbf{F}}_e \right) + \mathbb{F}_{ijk}(\mathbf{F}_e^\star) &= \mathbb{D}_{ijk} \left(\overset{\leftrightarrow}{\mathbf{F}}_v + \overset{\leftrightarrow}{\mathbf{F}}_a \right) + \mathbb{F}(\mathbf{F}_v^\star + \mathbf{F}_a^\star), \\ \mathcal{J}_{ijk} \overset{\leftrightarrow}{\mathbf{G}}_{ijk} &= \mathcal{M} \cdot \mathbb{D}_{ijk}^G(\mathbf{W}) + \mathbb{F}(\overset{\leftrightarrow}{\mathbf{W}}^\star), \end{aligned} \quad (\text{B3a})$$

$$\begin{aligned} \mathbb{D}_{ijk}(\vec{F}) &= \sum_{\alpha=0}^P (D_{i\alpha} - B_{i\alpha}) F_{\alpha jk} + \sum_{\alpha=0}^P (D_{j\alpha} - B_{j\alpha}) G_{i\alpha k} + \sum_{\alpha=0}^P (D_{k\alpha} - B_{k\alpha}) H_{ij\alpha}, \\ \mathbb{D}_{ijk}^\#(\vec{F}) &= \sum_{\alpha=0}^P (2D_{i\alpha} - B_{i\alpha}) F_{\alpha jk} + \sum_{\alpha=0}^P (2D_{j\alpha} - B_{j\alpha}) G_{i\alpha k} + \sum_{\alpha=0}^P (2D_{k\alpha} - B_{k\alpha}) H_{ij\alpha}, \\ \mathbb{D}_{ijk}^G(F) &= \left(\sum_{\alpha=0}^P (D_{i\alpha} - B_{i\alpha}) F_{\alpha jk}, \sum_{\alpha=0}^P (D_{j\alpha} - B_{j\alpha}) F_{i\alpha k}, \sum_{\alpha=0}^P (D_{k\alpha} - B_{k\alpha}) F_{ij\alpha} \right)^T, \\ \mathbb{F}_{ijk}(F^\star) &= \frac{F_{Njk}^\star l_i(1) - F_{0jk}^\star l_i(-1)}{\omega_i} + \frac{F_{iNk}^\star l_j(1) - F_{i0k}^\star l_j(-1)}{\omega_j} + \frac{F_{ijN}^\star l_k(1) - F_{ij0}^\star l_k(-1)}{\omega_k}, \end{aligned} \quad (\text{B3b})$$

where B is a matrix of zeros with $B_{00} = -1$ and $B_{PP} = 1$, and ω_i is the quadrature weight associated to the i -th node.

Appendix C: Tests with other variables

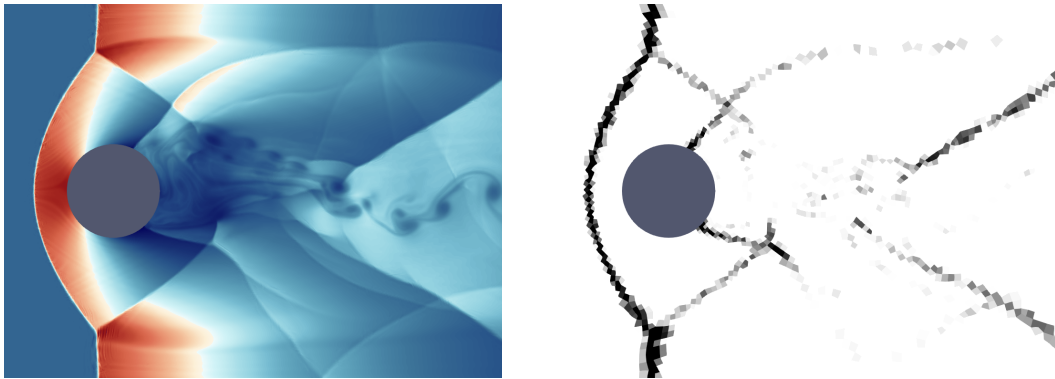
This section collects several results obtained for the cases of sections VIA and VIB with variables different from those proposed in the main text. The purpose of this appendix is first to show other alternatives that may work better when used in combination with numerical setups different from ours. And secondly, to give a deeper insight into alternative feature spaces and show why the variables chosen in this work perform well in both inviscid and viscous cases.

Figures 15 and 18 display the solution of the inviscid and viscous test cases, respectively, when using the modal sensor of section IVA. Both, p and ρ seem to give good results in the inviscid setup, with good sub-cell accuracy in the shocks and no dissipation in the wake. However, the discretization is over-dissipative for the viscous case, and the vortices

that appear behind the cylinder are not visible with these sensors. The simulation shows a steady flow that does not capture the physics of the problem.



(a) p with $s_0 = -3$ and $\Delta s = 1$.



(b) ρ with $s_0 = -3.5$ and $\Delta s = 1$.

FIG. 15. Inviscid case after 300,000 iterations with the modal sensor of section IV A.

The integral sensor of section IV B with the divergence of the velocity and the projection of the density gradient along the direction of the velocity also shows good results in the inviscid case of fig. 16. Some noise is generated at strong shocks, and this is more clear in the viscous case (Figure 19). With this configuration, the sensor cannot properly separate the shock waves from the boundary layer and therefore, we had to decrease its sensitivity to avoid detecting both. Dissipation in the main shock wave is not sufficient, and the oscillations travel downstream polluting the solution and interacting with the shock and vortices of the wake.

We finally discuss the performance of our GMM-based sensor under different choices of feature space. Using the work of 67 as a reference, we defined the following set of possible feature spaces:

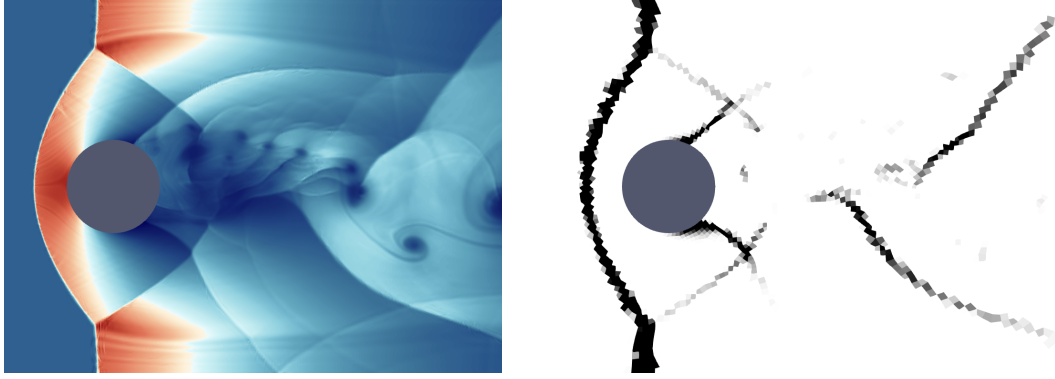
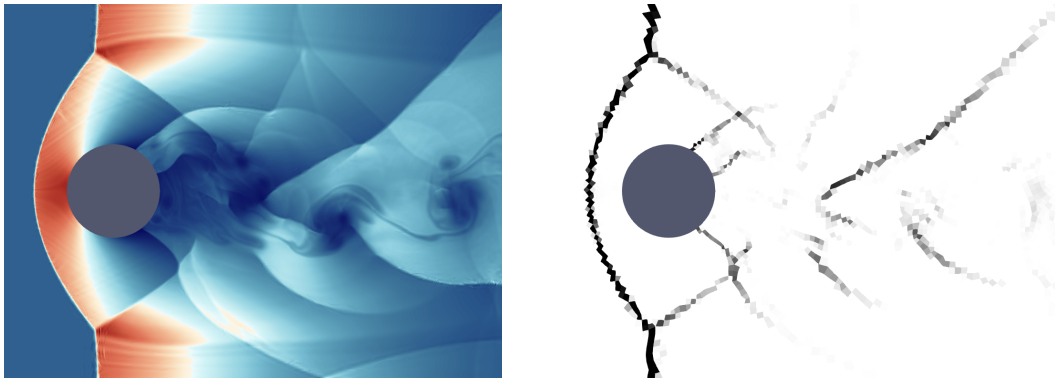

 (a) $(\nabla \cdot \vec{v})^2$ with $s_0 = 125$ and $\Delta s = 75$.

 (b) $\nabla \rho \cdot \vec{n}_v$ with $s_0 = 10.05$ and $\Delta s = 9.95$.

FIG. 16. Inviscid case after 300,000 iterations with the integral sensor of section IV B.

- $(\nabla \cdot \vec{v})^2$,
- $\vec{v} \cdot \vec{n}_p/a, (\nabla \cdot \vec{v})^2$,
- $\max(0, M - 1), (\nabla \cdot \vec{v})^2$,

where a is the speed of sound, \vec{n}_p is the unitary vector in the direction of the pressure gradient, and M is the Mach number. The results obtained with the inviscid flow (pictured in fig. 17) show that none of the variables considered in these tests is suitable for this setup, performing significantly better in the viscous case. The sensor that utilized the Mach number of the velocity in the direction of the pressure gradient was the only one that successfully completed the simulation, while the others crashed during the initial transient. And even in this case, it exhibited excessive dissipation.

The inherent viscosity of the flow at $\text{Re}=10^5$ seems to be beneficial for these sensors. With weaker oscillations and smoother shocks, they are able to properly detect the shock

regions, and they show an interesting behavior. Observing fig. 20, it is evident that the sensor featured in sub-figure a exhibits a higher sensitivity to discontinuities compared to the sensor in sub-figure b, which, in turn, demonstrates a greater sensitivity than the sensor in sub-figure c. In fact, the adaptive step of our approach removed some of the clusters for the last two sensors, meaning that the algorithm was not able to differentiate all the groups.

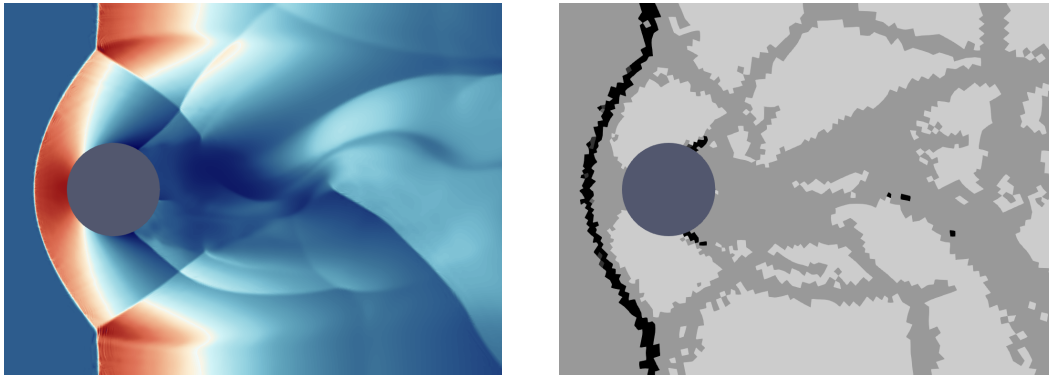
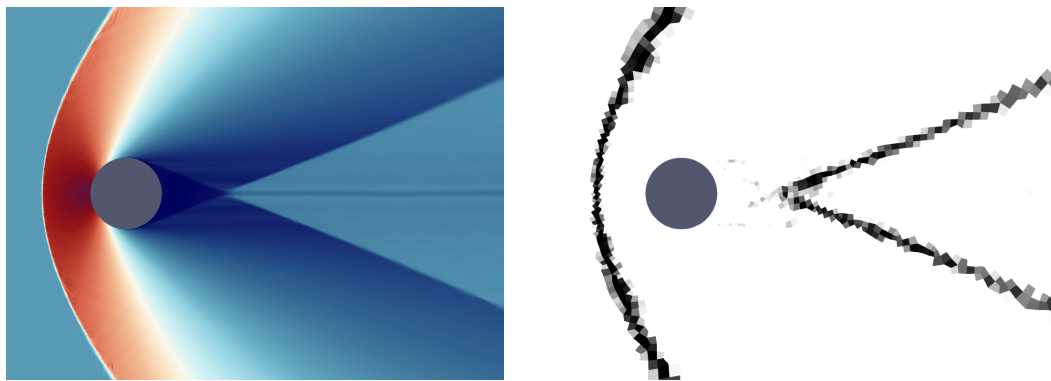


FIG. 17. Inviscid case after 300,000 iterations with our adaptive GMM sensor of section III using 6 clusters and the variables $\vec{v} \cdot \vec{n}_p/a, (\nabla \cdot \vec{v})^2$.

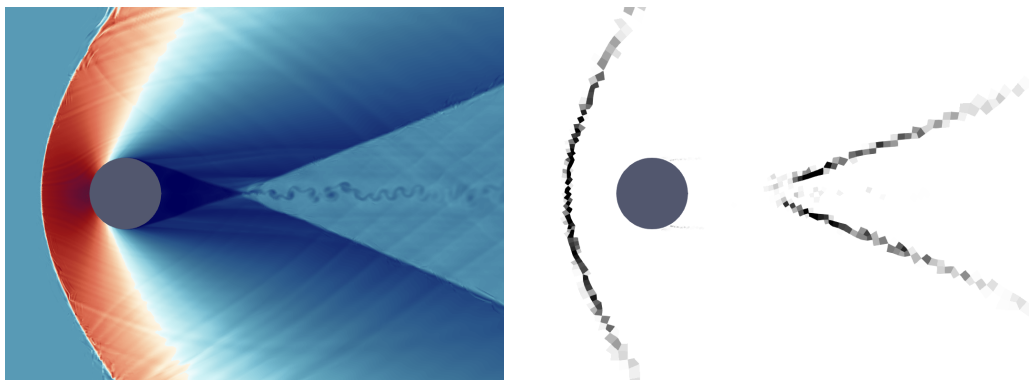


(a) p with $s_0 = -3.5$ and $\Delta s = 1$.

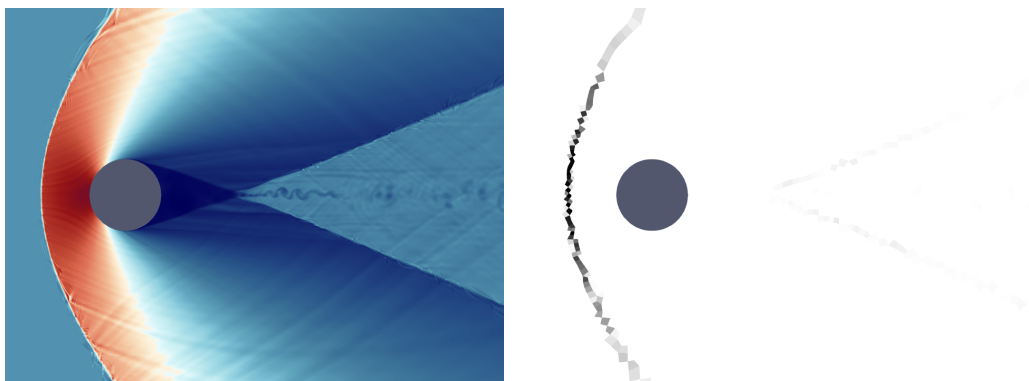


(b) ρ with $s_0 = -3.5$ and $\Delta s = 1$.

FIG. 18. Viscous case after 300,000 iterations with the modal sensor of section IV A.

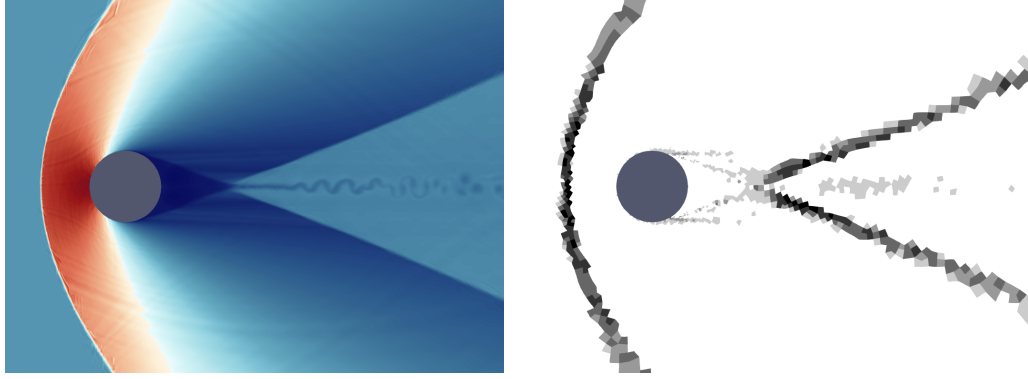


(a) $(\nabla \cdot \vec{v})^2$ with $s_0 = 125$ and $\Delta s = 75$.

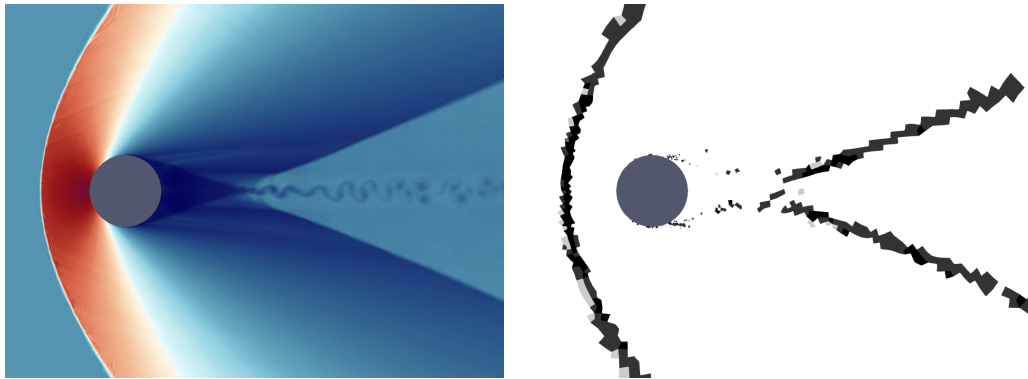


(b) $\nabla \rho \cdot \vec{n}_v$ with $s_0 = 15.05$ and $\Delta s = 14.95$.

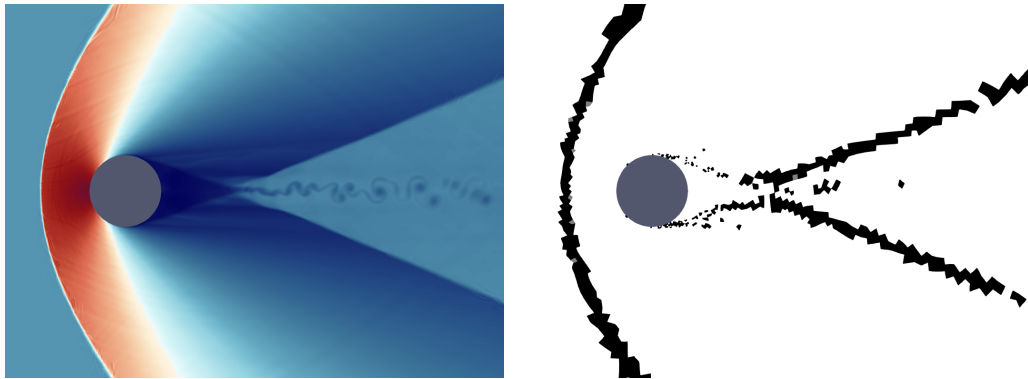
FIG. 19. Viscous case after 300,000 iterations with the integral sensor of section IV B.



(a) $(\nabla \cdot \vec{v})^2$.



(b) $\vec{v} \cdot \vec{n}_p/a, (\nabla \cdot \vec{v})^2$.



(c) $\max(0, M - 1), (\nabla \cdot \vec{v})^2$.

FIG. 20. Viscous case after 300,000 iterations with our adaptive GMM sensor of section III using 6 clusters. The simulation with the sensor based on $(\nabla \cdot \vec{v})^2$ was restarted from the 10,000th time step of the case using $\|\nabla p\|^2, (\nabla \cdot \vec{v})^2$.

REFERENCES

- ¹J. D. Anderson, Modern compressible flow: with historical perspective, Vol. 12, McGraw-Hill New York, 1990.
- ²S. Pirozzoli, Numerical methods for high-speed flows, Annual review of fluid mechanics 43 (2011) 163–194.
- ³R. Paciorri, A. Bonfiglioli, A shock-fitting technique for 2d unstructured grids, Computers & Fluids 38 (3) (2009) 715–726.
- ⁴M. Zahr, A. Shi, P.-O. Persson, Implicit shock tracking using an optimization-based high-order discontinuous galerkin method, Journal of Computational Physics 410 (2020) 109385. doi:10.1016/j.jcp.2020.109385.
URL <https://linkinghub.elsevier.com/retrieve/pii/S0021999120301595>
- ⁵A. Shi, P.-O. Persson, M. Zahr, Implicit shock tracking for unsteady flows by the method of lines, Journal of Computational Physics 454 (2022) 110906. doi:<https://doi.org/10.1016/j.jcp.2021.110906>.
URL <https://www.sciencedirect.com/science/article/pii/S0021999121008019>
- ⁶R. Eymard, T. Gallouët, R. Herbin, Finite volume methods, Handbook of numerical analysis 7 (2000) 713–1018.
- ⁷H. C. Yee, A class of high-resolution explicit and implicit shock-capturing methods, Tech. rep., NACA (1989).
- ⁸A. Harten, S. Osher, B. Engquist, S. R. Chakravarthy, Some results on uniformly high-order accurate essentially nonoscillatory schemes, Applied Numerical Mathematics 2 (3-5) (1986) 347–377.
- ⁹C.-W. Shu, S. Osher, Efficient implementation of essentially non-oscillatory shock-capturing schemes, Journal of computational physics 77 (2) (1988) 439–471.
- ¹⁰X.-D. Liu, S. Osher, T. Chan, Weighted essentially non-oscillatory schemes, Journal of computational physics 115 (1) (1994) 200–212.
- ¹¹G.-S. Jiang, C.-W. Shu, Efficient implementation of weighted eno schemes, Journal of computational physics 126 (1) (1996) 202–228.
- ¹²R. J. LeVeque, Finite volume methods for hyperbolic problems, Vol. 31, Cambridge university press, 2002.
- ¹³C.-W. Shu, High-order finite difference and finite volume weno schemes and discontinuous

- galerkin methods for cfd, *International Journal of Computational Fluid Dynamics* 17 (2) (2003) 107–118.
- ¹⁴T. Kossaczka, M. Ehrhardt, M. Günther, Enhanced fifth order weno shock-capturing schemes with deep learning, *Results in Applied Mathematics* 12 (2021) 100201. doi: <https://doi.org/10.1016/j.rinam.2021.100201>.
URL <https://www.sciencedirect.com/science/article/pii/S2590037421000431>
- ¹⁵B. Stevens, T. Colonius, Enhancement of shock-capturing methods via machine learning, *Theoretical and Computational Fluid Dynamics* 34 (4) (2020) 483–496.
- ¹⁶H. T. Huynh, A flux reconstruction approach to high-order schemes including discontinuous Galerkin methods, in: *18th AIAA Computational Fluid Dynamics Conference*, American Institute of Aeronautics and Astronautics, 2007. doi:10.2514/6.2007-4079.
URL <https://arc.aiaa.org/doi/abs/10.2514/6.2007-4079>
- ¹⁷P. E. Vincent, P. Castonguay, A. Jameson, A new class of high-order energy stable flux reconstruction schemes, *Journal of Scientific Computing* 47 (2011) 50–72.
- ¹⁸B. Cockburn, G. E. Karniadakis, C.-W. Shu, *Discontinuous Galerkin methods: theory, computation and applications*, Vol. 11, Springer Science & Business Media, 2012.
- ¹⁹B. Cockburn, S. Hou, C.-W. Shu, The runge-kutta local projection discontinuous galerkin finite element method for conservation laws. iv. the multidimensional case, *Mathematics of Computation* 54 (190) (1990) 545–581.
- ²⁰A. Burbeau, P. Sagaut, C.-H. Bruneau, A problem-independent limiter for high-order runge-kutta discontinuous galerkin methods, *Journal of Computational Physics* 169 (1) (2001) 111–150.
- ²¹J. Qiu, C.-W. Shu, Hermite weno schemes and their application as limiters for runge-kutta discontinuous galerkin method ii: Two dimensional case, *Computers & Fluids* 34 (6) (2005) 642–663.
- ²²J. Qiu, C.-W. Shu, A comparison of troubled-cell indicators for runge-kutta discontinuous galerkin methods using weighted essentially nonoscillatory limiters, *SIAM Journal on Scientific Computing* 27 (3) (2005) 995–1013.
- ²³D. S. Balsara, C. Altmann, C.-D. Munz, M. Dumbser, A sub-cell based indicator for troubled zones in rkdg schemes and a novel class of hybrid rkdg+ hweno schemes, *Journal of Computational Physics* 226 (1) (2007) 586–620.
- ²⁴M. Yang, Z.-J. Wang, A parameter-free generalized moment limiter for high-order methods

on unstructured grids, in: 47th AIAA Aerospace Sciences Meeting Including The New Horizons Forum and Aerospace Exposition, 2009, p. 605.

²⁵X. Zhong, C.-W. Shu, A simple weighted essentially nonoscillatory limiter for runge–kutta discontinuous galerkin methods, *Journal of Computational Physics* 232 (1) (2013) 397–415.

²⁶M. Dumbser, O. Zanotti, R. Loubère, S. Diot, A posteriori subcell limiting of the discontinuous galerkin finite element method for hyperbolic conservation laws, *Journal of Computational Physics* 278 (2014) 47–75.

²⁷G. Ntoukas, J. Manzanero, G. Rubio, E. Valero, E. Ferrer, A free-energy stable p-adaptive nodal discontinuous galerkin for the cahn-hilliard equation, *Journal of Computational Physics* 442 (2020) 110409.

²⁸G. Ntoukas, J. Manzanero, G. Rubio, E. Valero, E. Ferrer, An entropy-stable p-adaptive nodal discontinuous galerkin for the coupled navier-stokes/cahn-hilliard system, *Journal of Computational Physics* 458 (2021) 111093.

²⁹P. Mossier, A. Beck, C. D. Munz, A p-adaptive discontinuous galerkin method with hp-shock capturing, *Journal of Scientific Computing* 91 (1) (2022) 4.

³⁰S. Hennemann, A. M. Rueda-Ramírez, F. J. Hindenlang, G. J. Gassner, A provably entropy stable subcell shock capturing approach for high order split form dg for the compressible euler equations, *Journal of Computational Physics* 426 (2021) 109935. doi:<https://doi.org/10.1016/j.jcp.2020.109935>.

URL <https://www.sciencedirect.com/science/article/pii/S0021999120307099>

³¹A. M. Rueda-Ramírez, W. Pazner, G. J. Gassner, Subcell limiting strategies for discontinuous galerkin spectral element methods, *Computers & Fluids* 247 (2022) 105627. doi:<https://doi.org/10.1016/j.compfluid.2022.105627>.

URL <https://www.sciencedirect.com/science/article/pii/S0045793022002262>

³²A. Mateo-Gabín, A. M. Rueda-Ramírez, E. Valero, G. Rubio, A flux-differencing formulation with gauss nodes, *Journal of Computational Physics* 489 (2023) 112298. doi:<https://doi.org/10.1016/j.jcp.2023.112298>.

URL <https://www.sciencedirect.com/science/article/pii/S0021999123003935>

³³Y. Lin, J. Chan, High order entropy stable discontinuous galerkin spectral element methods through subcell limiting (2023). arXiv:2306.12663.

³⁴J. VonNeumann, R. D. Richtmyer, A method for the numerical calculation of hydrodynamic shocks, *Journal of applied physics* 21 (3) (1950) 232–237.

- ³⁵E. Tadmor, Convergence of spectral methods for nonlinear conservation laws, *SIAM Journal on Numerical Analysis* 26 (1) (1989) 30–44.
- ³⁶B.-y. Guo, H.-p. Ma, E. Tadmor, Spectral vanishing viscosity method for nonlinear conservation laws, *SIAM journal on numerical analysis* 39 (4) (2001) 1254–1268.
- ³⁷R. Hartmann, P. Houston, Adaptive discontinuous galerkin finite element methods for the compressible euler equations, *Journal of Computational Physics* 183 (2) (2002) 508–532.
- ³⁸P.-O. Persson, J. Peraire, Sub-cell shock capturing for discontinuous galerkin methods, in: 44th AIAA aerospace sciences meeting and exhibit, 2006, p. 112.
- ³⁹M. Feistauer, V. Kučera, J. Prokopová, Discontinuous galerkin solution of compressible flow in time-dependent domains, *Mathematics and Computers in simulation* 80 (8) (2010) 1612–1623.
- ⁴⁰G. E. Barter, D. L. Darmofal, Shock capturing with pde-based artificial viscosity for dgfm: Part i. formulation, *Journal of Computational Physics* 229 (5) (2010) 1810–1827.
- ⁴¹Y. Lv, Y. C. See, M. Ihme, An entropy-residual shock detector for solving conservation laws using high-order discontinuous galerkin methods, *Journal of Computational Physics* 322 (2016) 448–472.
- ⁴²F. Fraysse, C. Redondo, G. Rubio, E. Valero, Upwind methods for the baer-nunziato equations and higher-order reconstruction using artificial viscosity, *Journal of Computational Physics* 326 (2016) 805–827.
- ⁴³C. Redondo, F. Fraysse, G. Rubio, E. Valero, Artificial viscosity discontinuous galerkin spectral element method for the baer-nunziato equations, in: *Spectral and High Order Methods for Partial Differential Equations ICOSAHOM 2016: Selected Papers from the ICOSAHOM conference, June 27-July 1, 2016, Rio de Janeiro, Brazil*, Springer International Publishing, 2017, pp. 613–625.
- ⁴⁴J. Zeifang, A. Beck, A data-driven high order sub-cell artificial viscosity for the discontinuous galerkin spectral element method, *Journal of Computational Physics* 441 (2021) 110475. doi:<https://doi.org/10.1016/j.jcp.2021.110475>.
URL <https://www.sciencedirect.com/science/article/pii/S0021999121003703>
- ⁴⁵A. Mateo-Gabín, J. Manzanero, E. Valero, An entropy stable spectral vanishing viscosity for discontinuous galerkin schemes: Application to shock capturing and les models, *Journal of Computational Physics* 471 (2022) 111618. doi:[10.1016/j.jcp.2022.111618](https://doi.org/10.1016/j.jcp.2022.111618).
URL <https://linkinghub.elsevier.com/retrieve/pii/S0021999122006817>

- ⁴⁶A. Jameson, W. Schmidt, E. Turkel, Numerical solution of the euler equations by finite volume methods using runge kutta time stepping schemes, in: 14th fluid and plasma dynamics conference, 1981, p. 1259.
- ⁴⁷A. Klöckner, T. Warburton, J. S. Hesthaven, Viscous shock capturing in a time-explicit discontinuous galerkin method, *Mathematical Modelling of Natural Phenomena* 6 (3) (2011) 57–83.
- ⁴⁸A. Huerta, E. Casoni, J. Peraire, A simple shock-capturing technique for high-order discontinuous galerkin methods, *International journal for numerical methods in fluids* 69 (10) (2012) 1614–1632.
- ⁴⁹V. Rusanov, Processing and analysis of computation results for multidimensional problems of aerohydrodynamics, in: *Proceedings of the Third International Conference on Numerical Methods in Fluid Mechanics*, Springer, 1973, pp. 154–162.
- ⁵⁰E. Vorozhtsov, On shock localization by digital image processing techniques, *Comput. Fluids* 15 (1) (1987) 13–45.
- ⁵¹S.-P. Liou, A. Singh, S. Mehlig, D. Edwards, R. Davis, An image analysis based approach to shock identification in cfd, in: *33rd Aerospace Sciences Meeting and Exhibit*, 1995, p. 117.
- ⁵²Z. Wu, Y. Xu, W. Wang, R. Hu, Review of shock wave detection method in cfd post-processing, *Chin. J. Aeronaut.* 26 (3) (2013) 501–513.
- ⁵³A. Sheshadri, A. Jameson, Shock detection and capturing methods for high order discontinuous-galerkin finite element methods, in: *32nd AIAA Applied Aerodynamics Conference*, 2014, p. 2688.
- ⁵⁴S. L. Brunton, J. N. Kutz, *Data-Driven Science and Engineering: Machine Learning, Dynamical Systems, and Control*, Cambridge University Press, 2019.
- ⁵⁵P. Garnier, J. Viquerat, J. Rabault, A. Larcher, A. Kuhnle, E. Hachem, A review on deep reinforcement learning for fluid mechanics, *Computers & Fluids* 225 (2021) 104973.
- ⁵⁶R. Vinuesa, S. L. Brunton, Enhancing computational fluid dynamics with machine learning, *Nature Computational Science* 2 (6) (2022) 358–366.
- ⁵⁷M. Brenner, J. Eldredge, J. Freund, Perspective on machine learning for advancing fluid mechanics, *Physical Review Fluids* 4 (10) (2019) 100501.
- ⁵⁸S. L. Brunton, B. R. Noack, P. Koumoutsakos, Machine learning for fluid mechanics, *Annual review of fluid mechanics* 52 (2020) 477–508.

- ⁵⁹K. Fukami, K. Fukagata, K. Taira, Assessment of supervised machine learning methods for fluid flows, *Theoretical and Computational Fluid Dynamics* 34 (4) (2020) 497–519.
- ⁶⁰S. Le Clainche, E. Ferrer, S. Gibson, E. Cross, A. Parente, R. Vinuesa, Improving aircraft performance using machine learning: A review, *Aerospace Science and Technology* 138 (2023) 108354. doi:<https://doi.org/10.1016/j.ast.2023.108354>.
URL <https://www.sciencedirect.com/science/article/pii/S1270963823002511>
- ⁶¹M. H. Veiga, R. Abgrall, Towards a general stabilisation method for conservation laws using a multilayer perceptron neural network: 1d scalar and system of equations, in: ECCM - ECFD2018 6th European Conference on Computational Mechanics (Solids, Structures and Coupled Problems) 7th European Conference on Computational Fluid Dynamics, Glasgow, United Kingdom, 2018.
- ⁶²D. Ray, J. Hesthaven, An artificial neural network as a troubled-cell indicator, *J. Comput. Phys.* 367 (2018) 166–191.
- ⁶³D. Ray, J. Hesthaven, Detecting troubled-cells on two-dimensional unstructured grids using a neural network, *J. Comput. Phys.* 397 (2019) 108845.
- ⁶⁴N. Morgan, S. Tokareva, X. Liu, A. Morgan, A machine learning approach for detecting shocks with high-order hydrodynamic methods, in: *AIAA Scitech 2020 Forum*, 2020, p. 2024.
- ⁶⁵A. D. Beck, J. Zeifang, A. Schwarz, D. G. Flad, A neural network based shock detection and localization approach for discontinuous galerkin methods, *Journal of Computational Physics* 423 (2020) 109824. doi:<https://doi.org/10.1016/j.jcp.2020.109824>.
URL <https://www.sciencedirect.com/science/article/pii/S0021999120305982>
- ⁶⁶K.-E. Otmani, G. Ntoukas, O. A. Mariño, E. Ferrer, Toward a robust detection of viscous and turbulent flow regions using unsupervised machine learning, *Physics of Fluids* 35 (2) (2023) 027112.
- ⁶⁷E. Saetta, R. Tognaccini, Identification of flowfield regions by machine learning, *AIAA Journal* 61 (4) (2023) 1503–1518. arXiv:<https://doi.org/10.2514/1.J061907>, doi: 10.2514/1.J061907.
URL <https://doi.org/10.2514/1.J061907>
- ⁶⁸K. Tlales, K. E. Otmani, G. Ntoukas, G. Rubio, E. Ferrer, Machine learning adaptation for laminar and turbulent flows: applications to high order discontinuous galerkin solvers, arXiv preprint arXiv:2209.02401 (2022).

- ⁶⁹K. Black, A conservative spectral element method for the approximation of compressible fluid flow, *Kybernetika* 35 (1999).
- ⁷⁰D. A. Kopriva, *Implementing spectral methods for partial differential equations: Algorithms for scientists and engineers*, Springer Science & Business Media, 2009.
- ⁷¹E. Ferrer, G. Rubio, G. Ntoukas, W. Laskowski, O. Mariño, S. Colombo, A. Mateo-Gabín, H. Marbona, F. M. de Lara, D. Huergo, J. Manzanero, A. Rueda-Ramírez, D. Kopriva, E. Valero, Horses3d: A high-order discontinuous galerkin solver for flow simulations and multi-physics applications, *Computer Physics Communications* 287 (2023) 108700. doi:10.1016/J.CPC.2023.108700.
- ⁷²G. J. Gassner, A. R. Winters, F. J. Hindenlang, D. A. Kopriva, The BR1 scheme is stable for the compressible Navier-Stokes equations, *Journal of Scientific Computing* 77 (2018) 154–200. doi:10.1007/s10915-018-0702-1.
URL <https://doi.org/10.1007/s10915-018-0702-1>
- ⁷³J. L. Guermond, B. Popov, Viscous regularization of the Euler equations and entropy principles, *SIAM Journal on Applied Mathematics* 74 (2014) 284–305. doi:10.1137/120903312.
- ⁷⁴P.-O. Persson, J. Peraire, Sub-cell shock capturing for discontinuous galerkin methods, *Collection of Technical Papers - 44th AIAA Aerospace Sciences Meeting 2* (2006) 1408–1420. doi:10.2514/6.2006-112.
- ⁷⁵E. Tadmor, Entropy stability theory for difference approximations of nonlinear conservation laws and related time-dependent problems, *Acta Numerica* 12 (2003) 451–512. doi:10.1017/S0962492902000156.
- ⁷⁶X. Zhang, C.-W. Shu, Maximum-principle-satisfying and positivity-preserving high-order schemes for conservation laws: survey and new developments, *Journal of Computational Physics* 467 (2011) 3091–3120. doi:10.1098/rspa.2011.0153.
URL <https://royalsocietypublishing.org/>
- ⁷⁷F. Bassi, S. Rebay, A high-order accurate discontinuous finite element method for the numerical solution of the compressible Navier–Stokes equations, *Journal of Computational Physics* 131 (1997) 267–279. doi:10.1006/JCPH.1996.5572.
- ⁷⁸P. Chandrashekar, Kinetic energy preserving and entropy stable finite volume schemes for compressible Euler and Navier-Stokes equations, *Communications in Computational Physics* 14 (2013) 1252–1286. doi:10.4208/cicp.170712.010313a.

- ⁷⁹F. Ismail, P. L. Roe, Affordable, entropy-consistent Euler flux functions II: Entropy production at shocks, *Journal of Computational Physics* 228 (2009) 5410–5436. doi:10.1016/j.jcp.2009.04.021.
- ⁸⁰M. Maier, M. Kronbichler, Efficient parallel 3d computation of the compressible euler equations with an invariant-domain preserving second-order finite-element scheme, *ACM Transactions on Parallel Computing* 8 (3) (2021) 16:1–30. doi:10.1145/3470637.
URL <https://arxiv.org/abs/2007.00094>
- ⁸¹F. E. Gowen, E. W. Perkins, Drag of circular cylinders for a wide range of reynolds numbers and mach numbers, Tech. rep., NACA (6 1952).
URL <https://ntrs.nasa.gov/citations/19930087134>
- ⁸²V. A. Bashkin, I. V. Egorov, M. V. Egorova, D. V. Ivanov, Supersonic laminar-turbulent gas flow past a circular cylinder, *Fluid Dynamics* 35 (2000) 652–662. doi:10.1023/A:1026630613133.
URL <https://link.springer.com/article/10.1023/A:1026630613133>
- ⁸³V. A. Bashkin, A. V. Vaganov, I. V. Egorov, D. V. Ivanov, G. A. Ignatova, Comparison of calculated and experimental data on supersonic flow past a circular cylinder, *Fluid Dynamics* 37 (2002) 473–483. doi:10.1023/A:1019675027402/METRICS.
URL <https://link.springer.com/article/10.1023/A:1019675027402>
- ⁸⁴F. Pedregosa, G. Varoquaux, A. Gramfort, V. Michel, B. Thirion, O. Grisel, M. Blondel, P. Prettenhofer, R. Weiss, V. Dubourg, J. Vanderplas, A. Passos, D. Cournapeau, M. Brucher, M. Perrot, E. Duchesnay, Scikit-learn: Machine learning in Python, *Journal of Machine Learning Research* 12 (2011) 2825–2830.
- ⁸⁵G. J. Gassner, A. R. Winters, D. A. Kopriva, Split form nodal discontinuous galerkin schemes with summation-by-parts property for the compressible euler equations, *Journal of Computational Physics* 327 (2016) 39–66. doi:10.1016/J.JCP.2016.09.013.